Paleoceanography and Paleoclimatology

AGU ADVANCING EARTH AND SPACE SCIENCE

RESEARCH ARTICLE
10.1029/2022PA004577

Key Points:

- Earth system's response to weathering changes is probed in 600,000 year-long simulations with the Bern3D model and a cost-efficient emulator
- Equilibration timescales are on the order 10,000 years for CO_2 and 100,000 years for $\delta^{13}C$, requiring careful model initialization
- Literature-based weathering scenarios for the past 800,000 years reveal significant responses in CO_2, carbonate ion, and $\delta^{13}C$

Supporting Information:

Supporting Information may be found in the online version of this article.

Correspondence to:

A. Jeltsch-Thömmes,
aurich.jeltsch-thoemmes@unibe.ch

Citation:

Jeltsch-Thömmes, A., & Joos, F. (2023). Carbon cycle responses to changes in weathering and the long-term fate of stable carbon isotopes. *Paleoceanography and Paleoclimatology*, *38*, e2022PA004577. https://doi.org/10.1029/2022PA004577

Received 7 NOV 2022
Accepted 31 JAN 2023

Carbon Cycle Responses to Changes in Weathering and the Long-Term Fate of Stable Carbon Isotopes

A. Jeltsch-Thömmes[1] and F. Joos[1]

[1]Climate and Environmental Physics, Physics Institute and Oeschger Centre for Climate Change Research, University of Bern, Bern, Switzerland

Abstract The causes of CO_2 variations over the past million years remain poorly understood. Imbalances between the input of elements from rock weathering and their removal from the atmosphere-ocean-biosphere system to the lithosphere likely contributed to reconstructed changes. We employ the Bern3D model to investigate carbon-climate responses to step-changes in the weathering input of phosphorus, alkalinity, carbon, and carbon isotope ratio ($\delta^{13}C$) in simulations extending up to 600,000 years. CO_2 and climate approach a new equilibrium within a few ten thousand years, whereas equilibrium is established after several hundred thousand years for $\delta^{13}C$. These timescales represent a challenge for the initialization of sediment-enabled models and unintended drifts may be larger than forced signals in simulations of the last glacial–interglacial cycle. Changes in dissolved CO_2 change isotopic fractionation during marine photosynthesis. This causes distinct spatio-temporal perturbations in $\delta^{13}C$ and affects the burial flux of ^{13}C. We force a cost-efficient emulator, based on the Bern3D results, with contrasting literature-based weathering histories over the last 800 thousand years. Glacial–interglacial amplitudes of up to 30 ppm in CO_2, 0.05‰ in $\delta^{13}C$, and ∼15 mmol m^{-3} in deep ocean CO_3^{2-} are emulated for changes in carbonate rock weathering. Plausible input from the decomposition of organic matter on shelves causes variations of up to 10 ppm in CO_2, 0.09‰ in $\delta^{13}C$, and 5 mmol m^{-3} in CO_3^{2-}, highlighting the non-negligible effect of weathering-burial imbalances.

Plain Language Summary Data from ice cores and marine sediments document large changes in atmospheric carbon dioxide (CO_2) and climate during the past million years. Carbon isotopes and other proxies can help to understand underlying processes. In this study, we investigate Earth's response to plausible changes in the input of carbon and other elements from the weathering of rocks or the decomposition of previously accumulated organic matter with the help of a computer model. Results show significant variations in CO_2, carbon isotopes, marine chemistry, marine biological productivity, and burial fluxes of biogenic particles to the lithosphere. The adjustment time to changes in input flux is several ten thousand years for CO_2 and climate, and several hundred thousand years for carbon isotopes. As it is computationally challenging to simulate such long time periods with complex models, we used our results to build an emulator. Such emulators, representing the responses of spatially resolved and process-based models, are useful for studies addressing Earth's history over many millions of years. Simulating a million years with the emulator takes seconds, whereas it takes about 4 months with the complex model. In conclusion, our work highlights the role of weathering fluxes and their possible contribution to past climate-carbon cycle swings.

1. Introduction

Chemical weathering of rocks and deposits eventually provides a continuous flow of carbon and other elements to the ocean (e.g., Berner, 1990; Compton et al., 2000; Hartmann et al., 2014; Lacroix et al., 2021; Suchet & Probst, 1995; Walker et al., 1981), thereby influencing climate, atmospheric CO_2, carbon isotopes, biogeochemical cycles, and the oxidative capacity at the Earth's surface on millennial and longer time scales (Hayes & Waldbauer, 2006; Kump & Alley, 1994). However, Earth's system responses to changes in weathering remain uncertain, and their representation in Earth system simulations extending over many thousands or even millions of years computationally challenging.

Proxy records show climate and biogeochemical cycles to vary on orbital time scales (Lisiecki, 2014; Lisiecki & Raymo, 2005). Over the past 800 thousand years (Kyr), ice core records document past changes in atmospheric CO_2, which varied between 180 and 300 ppm (e.g., Bereiter et al., 2015; Lüthi et al., 2008; Marcott et al., 2014; Neftel et al., 1982; Siegenthaler et al., 2005), and in its stable carbon isotope ratio, $\delta^{13}C_{atm}$ ($^{13}C/^{12}C$ in permil

units), (e.g., Eggleston et al., 2016; Lourantou et al., 2010; Schmitt et al., 2012; Schneider et al., 2013). Variations in the greenhouse gas CO_2 strongly contributed to glacial–interglacial climate swings and $\delta^{13}C$ records constrain related biogeochemical processes. Marine records of $\delta^{13}C$ (e.g., Hoogakker et al., 2006; Lisiecki, 2014; Oliver et al., 2010; C. D. Peterson & Lisiecki, 2018; C. D. Peterson et al., 2014; Raymo et al., 1997; Schmittner et al., 2013), carbonate preservation (e.g., L. C. Peterson & Prell, 1985), and other proxies reach further back in time and cover the Pleistocene epoch, although with partly sparse spatial coverage and lower temporal resolution. A multitude of processes has been proposed to explain these variations. The processes involve, besides changes in the physical Earth system, changes in the marine and terrestrial carbon cycle, ocean-sediment interactions, and changes in terrestrial weathering (e.g., Archer, Winguth, & Pierrehumbert, 2000; Fischer et al., 2010; Jaccard et al., 2013; Jeltsch-Thömmes et al., 2019; Menviel et al., 2012; Sigman & Boyle, 2000; Sigman et al., 2010; Wallmann et al., 2016).

Weathering fluxes enter the ocean through riverine transport in the form of dissolved inorganic and organic compounds and particulate organic matter (POM) (Lacroix et al., 2021; Meybeck, 1982; Regnier et al., 2013; Tréguer et al., 2021). For example, phosphorus is primarily delivered to the ocean as particulate organic phosphate, mediated by land biosphere processes, and attached to surfaces of iron-manganese and hydroxide particles, in addition to dissolved inorganic and dissolved organic phosphorus (Compton et al., 2000; Lacroix et al., 2021). Estimates suggest that there are weathering hotspots and that 70% of today's global weathering fluxes derive from only 10% of the land area (Hartmann et al., 2014). Carbon is also released to the climate system via outgassing of magmas at seafloor hydrothermal vents, hot-spot and island arc volcanoes, and by other forms of volcanism (Hayes & Waldbauer, 2006). Chemical weathering rates are thought to be governed by lithology, hydrology and runoff, rates of physical erosion, soil properties and shielding of rocks by soils, and temperature (e.g., Colbourn et al., 2013; Hartmann et al., 2014). All these parameters changed over glacial–interglacial cycles and Earth's history.

The input of carbon and nutrients from the lithosphere is roughly balanced by the burial of biogenic particles and other material in the lithosphere, yet imbalances remain. For example, the input by weathering and the input-burial balance was strongly perturbed over past glacial–interglacial cycles (Broecker & Peng, 1987; Cartapanis et al., 2016, 2018; Kump & Alley, 1994; L. C. Peterson & Prell, 1985). Input-burial imbalances directly affect the inventories and concentrations of carbon, nutrients, and alkalinity in the ocean. In turn, the production and burial of biogenic particles are changing.

The burial of biogenic particles is mediated by the marine carbon and biogeochemical cycles (e.g., Emerson & Bender, 1981; Sarmiento & Gruber, 2006; Tschumi et al., 2011). Marine ecosystems remove dissolved inorganic carbon (DIC), nutrients, and alkalinity from surface waters to eventually generate dissolved organic matter and particles of calcium carbonate ($CaCO_3$), opal, and organic matter. The particles sink through the water column toward the ocean floor. This biogenic material is mainly remineralized to DIC and inorganic nutrients within the water column and surface (reactive) sediments, but a fraction is buried in consolidated sediments. Rates of particle sinking, remineralization, and burial depend on particle size and composition, and environmental parameters. These parameters include, for example, temperature, oxygen, viscosity, or the saturation state of water for $CaCO_3$ in the water column and reactive sediments. Large amounts of carbon and nutrients get buried in organic forms in the coastal zone and on continental shelves (Regnier et al., 2013; Wallmann et al., 2016). This material may be released again from exposed shelves during low glacial sea level and contribute, together with changes in weathering and burial, to imbalances between fluxes from and to the lithosphere (Wallmann, 2014; Wallmann et al., 2016). Changes in surface ocean DIC and alkalinity from input-burial imbalances and altered particle cycling change atmospheric CO_2, forcing climate to change. Input-burial imbalances also strongly affect $\delta^{13}C$ of carbon in the atmosphere, ocean, ocean sediments, and the land biosphere (Broecker, 1970; Jeltsch-Thömmes & Joos, 2020; Komar & Zeebe, 2021; Mills et al., 2017; Roth et al., 2014; Schrag et al., 2013).

Modeling the responses to input-burial imbalances is computationally challenging. The response time scales to input-burial imbalances range from several millennia to hundreds of thousands of years for CO_2 (e.g., Archer et al., 1998; Colbourn et al., 2015) and $\delta^{13}C$ (Jeltsch-Thömmes & Joos, 2020; Roth et al., 2014). Spatial gradients within the ocean are important and influence, for example, the isotopic composition of the burial flux of organic and $CaCO_3$ particles into the lithosphere (Jeltsch-Thömmes & Joos, 2020). Earlier model studies on glacial–interglacial change considered the effect of sedimentary carbonate burial and dissolution on perturbations in atmospheric CO_2, but typically neglected organic matter burial (e.g., Archer & Maier-Reimer, 1994; Archer, Winguth, Lea, & Mahowald, 2000; Broecker & Peng, 1987, 1989; Brovkin et al., 2012; Emerson & Archer, 1992;

Ganopolski & Brovkin, 2017; Sigman & Boyle, 2000; Sigman et al., 1998, 2010; Willeit et al., 2019). Further studies show that feedbacks between organic matter burial, marine nutrient concentrations, and biological productivity are important (Cartapanis et al., 2018; Jeltsch-Thömmes et al., 2019; Komar & Zeebe, 2021; Menviel et al., 2012; Tschumi et al., 2011) and can strongly amplify perturbations in atmospheric CO_2 on glacial–interglacial time scales (Roth et al., 2014). Input-burial imbalances arising from changes in the burial fluxes of opal and carbonate or the weathering rates of silicate and carbonate rocks (e.g., Börker et al., 2020; Clark et al., 2006; Köhler & Munhoven, 2020; Munhoven, 2002; Munhoven & François, 1996; Willeit et al., 2019), or changes in CO_2 outgassing associated with volcanism (Huybers & Langmuir, 2009; Roth & Joos, 2012) have been invoked as possible contributing processes to explain glacial–interglacial variations and the Neogene cooling (23–2.6 million years ago) (e.g., Caves et al., 2016; Rugenstein et al., 2019). On even longer timescales, covering Earth's history, the coupled carbon-silica cycle is thought to stabilize climate on Earth via negative feedbacks in weathering of carbonate and silicate rocks (e.g., Berner, 1990; Isson et al., 2020; Kasting, 2019; Ridgwell & Zeebe, 2005; Stolper et al., 2016; Walker et al., 1981). Net organic matter accumulation in sediments and the accumulation of the oxidizing capacity at Earth's surface is reconstructed from $\delta^{13}C$ recorded in carbonate deposits (Broecker, 1970; Mills et al., 2017; Schrag et al., 2013). Models applied to quantitatively interpret the $\delta^{13}C$ carbonate records typically treat the fast exchanging reservoirs (atmosphere, ocean, ocean sediments, and land biosphere) as a single boxes to facilitate long simulations (Bergman et al., 2004; Berner, 2006).

Cost-efficient substitute models, which capture the spatial and temporal responses of more complex models, could be constructed and applied to study input-burial imbalances instead of box models. The substitute (or emulator) can be used to explore responses over long time scales or to run many sensitivity studies, which are computationally inaccessible with more comprehensive and therefore more expensive models. The spatio-temporal response of a complex model, its Green's function, can be captured in an idealized model simulation where the forcing is changed in a step- or pulse-like manner (e.g., Bastiaansen et al., 2021; Hooss et al., 2001; Joos & Bruno, 1996; Joos et al., 2013; Maier-Reimer & Hasselmann, 1987; Metzler et al., 2018; Strassmann & Joos, 2018; Thompson & Randerson, 1999). Idealized response simulations allow for a better understanding of underlying processes as they reveal the characteristic timescales and spatial patterns of the system's adjustment to an external perturbation, for example, a change in weathering. While the processes and timescales affecting CO_2 have been investigated in several step-change experiments (e.g., Archer & Maier-Reimer, 1994; Sigman et al., 1998; Tschumi et al., 2011), to our knowledge no studies so far have systematically investigated the effect of changes in weathering input fluxes on both, carbon and carbon isotope budgets.

Here, we use the Bern3D Earth system model of intermediate complexity to perform idealized, up to 600 Kyr long simulations. The weathering input fluxes of alkalinity, nutrients, carbon, and $\delta^{13}C$ are changed in a step-wise manner. The aim is to generate Green's functions and to understand the spatial and temporal responses in carbon inventories and $\delta^{13}C$ in the atmosphere and ocean, and changes in marine biogeochemical cycling as well as the evolution of input-burial imbalances. Section 2 details the model and experimental setup. In Section 3 we quantify the contribution to the carbon and carbon isotopic perturbations from the organic carbon and $CaCO_3$ cycles and highlight the role of vertical gradients in $\delta^{13}C$ in the ocean based on the Bern3D model results. In Section 4 we discuss the uncertainties and limitations of our approach and use the response to step-changes in the input of $CaCO_3$ and organic material as simulated with the Bern3D model to build a cost-efficient substitute model to simulate the response in CO_2, CO_3^{2-}, and $\delta^{13}C_{DIC}$ to different weathering scenarios over the past 800 Kyr. Finally, in Section 5 a summary and conclusions are provided.

2. Model Description and Experimental Set Up

2.1. Model Description

The Bern3D v2.0s intermediate complexity model couples a single layer energy-moisture balance atmosphere with a thermodynamic sea-ice component (Ritz et al., 2011), a 3D geostrophic-frictional balance ocean (Edwards et al., 1998; Müller et al., 2006) with an isopycnal diffusion scheme and Gent-McWilliams parameterization for eddy-induced transport (Griffies, 1998), and a 10-layer ocean sediment module (Heinze et al., 1999; Jeltsch-Thömmes et al., 2019; Tschumi et al., 2011). The horizontal resolution across Bern3D model components is 41 × 40 grid cells and 32 logarithmically spaced depth layers in the ocean (Roth et al., 2014). Wind stress is prescribed from the NCEP/NCAR monthly wind stress climatology (Kalnay et al., 1996), and gas exchange at the ocean surface and calculation of carbonate chemistry follow OCMIP-2 protocols (Najjar & Orr, 1999; Orr &

Epitalon, 2015; Wanninkhof, 2014), with an adjusted gas transfer dependency on wind speed (Müller et al., 2008). In the ocean, marine productivity is restricted to the euphotic zone (75 m) and calculated as a function of light availability, temperature, and nutrient concentrations (Fe, P, Si) and used to compute the export of dissolved and POM, with a constant elemental ratio for P:ALK:C:O_2 (1:17:117:−170), and the export of opal and calcium carbonate ($CaCO_3$), pending on dissolved silica and an upper limit $CaCO_3$ to particulate organic carbon (POC) export ratio of 0.083 (Parekh et al., 2008; Tschumi et al., 2011). Remineralization of particle fluxes follows fixed scalings with depth.

The sediment module covers the top 10 cm and dynamically calculates the transport, dissolution, and bioturbation, and burial of solid material (POM, $CaCO_3$, opal, clay), and the pore water chemistry, and diffusion of DIC, $DI^{13}C$, $DI^{14}C$, alkalinity, phosphate, oxygen, and silic acid (Jeltsch-Thömmes et al., 2019; Tschumi et al., 2011). Dissolution rates depend on pore water concentrations. The P:C ratio of POM is conserved in the standard setup. Burial (loss) of phosphorus, silica, carbon, and alkalinity from the sediment to the lithosphere is balanced by a variable input flux to the coastal surface ocean during spin-up. These weathering input fluxes are set equal to burial fluxes at the end of the spin-up for transient simulations. Iron is added to the model ocean by prescribed fluxes from aeolian deposition and continental margins and removed by particle scavenging (Parekh et al., 2008). Iron is not included in the sediment module.

The model is coupled to a 4-box representation of the land-biosphere carbon reservoirs (Siegenthaler & Oeschger, 1987). Here, the only purpose of this 4-box carbon reservoir model is to represent the dilution of atmospheric isotopic perturbations by the land biosphere, while other processes and changes in land carbon stocks are not considered. In other words, the land-biosphere carbon pool sizes are constant, but their $\delta^{13}C$ signature changes, depending on changes in $\delta^{13}C_{atm}$.

For a detailed description of the Bern3D model version used here, the reader is referred to Appendix A of Jeltsch-Thömmes et al. (2019).

2.2. Implementation of ^{13}C in the Model

^{13}C is implemented as a tracer in all Bern3D model components such that ^{13}C fluxes and inventories can be explicitly simulated across the atmosphere-ocean-land biosphere-reactive ocean sediments (AOBS) system. Fractionation of ^{13}C is considered for atmosphere-ocean gas transfer, carbonate chemistry, the formation of $CaCO_3$, POC and dissolved organic carbon, and during photosynthesis on land. Fractionation during photosynthesis on land is kept fixed; the simple 4-box model, applied here for computational reasons, does not represent changes in C3 and C4 plants nor changes in their discrimination. This is an uncertainty. No fractionation is considered for the remineralization of organic carbon in the ocean and on land. Formulations on how fractionation is calculated and corresponding references are summarized in Table 1.

2.3. Implementation of Weathering Input Fluxes in the Model

The loss of carbon (C), silica (Si), alkalinity (ALK), and phosphorus (P) from the open ocean through sedimentary burial is counteracted by the input of weathered material to the open ocean. In the model, this is implemented in an idealized way: the loss fluxes of tracers through burial of material in the lithosphere are, in steady state, balanced by input fluxes of equal size. The elemental ratios (^{12}C:^{13}C:Si:ALK:P) of the input flux to the open ocean are therefore dictated by the elemental ratios of the global burial flux at the end of the spin up. Throughout the manuscript, these fluxes to the ocean will be referred to as input fluxes.

C, Si, P, and ALK input are uniformly added to the corresponding dissolved inorganic tracer concentrations of the near-coastal surface grid cells in Bern3D. Thus, we do not represent reprocessing of elements, for example, by the land biosphere or in estuaries, nor different forms of input such as dissolved and POM, or P attached to surfaces of iron-manganese and hydroxide particles (Compton et al., 2000; Lacroix et al., 2021). Atmospheric deposition of C, Si, ALK, and P may be viewed as included in the input fluxes. This simplification appears justified as the different forms of input eventually enter the inorganic pools on time scales shorter than the multi-millennial timescales addressed in this study. We attribute the elemental input fluxes conceptually to different processes such as silicate and carbonate weathering.

Table 1
Equations Describing the Fractionation in the Model

Domain	Formulation
Air-sea[a,b]	$\alpha_{a\to s} = (1 - 0.0005 - 0.0002) \cdot \left(1 - \frac{0.373}{T} + 0.00019\right)$
Carbonate chemistry[b]	$\alpha_{CO_{2,aq}\leftrightarrow HCO_3^-} = \left(1 - \frac{9.866}{T} + 0.02412\right)$
	$\alpha_{HCO_3^-\leftrightarrow CO_3^{2-}} = \left(1 - \frac{0.867}{T} + 0.00252\right)$
	$\alpha_{CO_{2,aq}\leftrightarrow DIC} = \frac{DIC}{[CO_{2,aq}] + \frac{[HCO_3^-]}{\alpha_{CO_{2,aq}\leftrightarrow HCO_3^-}} + \frac{[CO_3^{2-}]\cdot\alpha_{HCO_3^-\leftrightarrow CO_3^{2-}}}{\alpha_{CO_{2,aq}\leftrightarrow HCO_3^-}}}$
Sea-air[b]	$\alpha_{s\to a} = (1 - 0.0005 - 0.0002) \cdot \alpha_{CO_{2,aq}\leftrightarrow DIC}$
$CaCO_3$ formation[b]	$\alpha_{HCO_3^-\to CaCO_3} = \left(1 - \frac{4.232}{T} + 0.0151\right)$
Marine photosynthesis[c]	$\alpha_{[CO_2]\to C_{org}} = \left(1.00119 + 0.01203 \cdot \log_{10}\left([CO_{2,aq}]\right)\right)$
Terrestrial photosynthesis[d]	Constant fractionation of −18.1‰

Note. T denotes sea surface temperature in Kelvin, and $[CO_{2,aq}]$ aqueous CO_2 in μmol kg^{-1}.
[a]Siegenthaler and Muennich (1981). [b]Mook (1986). [c]Freeman and Hayes (1992). [d]Siegenthaler and Oeschger (1987).

Input from 1 mol $CaSiO_3$ adds 1 mol of Si, 2 mol of alkalinity, and no carbon to the model ocean. This is a short-circuit of the atmosphere following the simplified reaction for weathering of tectosilicates (e.g., Colbourn et al., 2013):

$$2CO_{2(aq)} + H_2O + CaSiO_{3(s)} \rightarrow Ca^{2+}_{(aq)} + 2HCO^-_{3(aq)} + SiO_{2(aq)} \quad (1)$$

Two moles of carbon are removed from the atmosphere-ocean system in the form of CO_2 and 2 mol of alkalinity and carbon in the form of HCO_3^- are added to the ocean. On the timescales considered here, the atmosphere and surface ocean can be considered well mixed and we do not represent the outgassing of CO_2 and the related interhemispheric ocean carbon transport arising from the riverine carbon inputs (Lacroix et al., 2020; Sarmiento et al., 1992).

Weathering of carbonate rocks ($CaCO_3$) is given by (e.g., Goodwin & Ridgwell, 2010):

$$CaCO_{3(s)} + CO_{2(aq)} + H_2O \rightarrow Ca^{2+}_{(aq)} + 2HCO^-_{3(aq)}. \quad (2)$$

In the model, 2 mol of alkalinity for each mole of carbon are added. This is again a short-circuit of the atmosphere.

Input fluxes (F) of P, Si, ALK, DIC, and $^{13}C_{DIC}$ are attributed to the weathering flux from carbonate rocks, F_{CaCO_3}, silicate rocks, F_{CaSiO_3}, an assumed conceptual input flux releasing the elements of former organic material, F_{org} (from hereon referred to as organic input flux), and a remainder flux, $F_{remainder}$, to close the carbon and carbon isotopic budget of the model in equilibrium. $F_{remainder}$ is thought of as CO_2 emissions from volcanism and tectonic outgassing. The input F_{org} should not be confused with a flux of organic material as all input fluxes are added to the inorganic tracer pools in Bern3D. At steady state, the global elemental fluxes of F_{org} are equal to those of the global burial flux of POM. The fluxes are related to each other in molar units:

$$F_P = \mathcal{R}_{P:C} \cdot F_{org} \quad (3)$$

$$F_{Si} = F_{CaSiO_3} \quad (4)$$

$$F_{ALK} = 2 \cdot F_{CaSiO_3} + 2 \cdot F_{CaCO_3} + \mathcal{R}_{ALK:P} \cdot \mathcal{R}_{P:C} \cdot F_{org} \quad (5)$$

$$F_{DIC} = F_{CaCO_3} + F_{org} + F_{remainder} \quad (6)$$

$$F_{DIC\text{-}13} = F_{CaCO_3} \cdot {}^{13}R_{CaCO_3} + F_{org} \cdot {}^{13}R_{org} + F_{remainder} \cdot {}^{13}R_{remainder} \quad (7)$$

$\mathcal{R}_{P:C}$ and $\mathcal{R}_{ALK:P}$ are the Redfield ratios of P:C = 1:117 and ALK:P = −17:1, respectively (L. A. Anderson & Sarmiento, 1994; Paulmier et al., 2009). ^{13}R denotes the $^{13}C/C$ isotopic ratio.

Table 2
Export, Deposition, and Burial Fluxes of $CaCO_3$, Opal, and Particulate Organic Carbon (POC), Carbon and Opal Inventories and the Respective $\delta^{13}C$ Signatures (Note That Atmospheric CO_2 and Its $\delta^{13}C$ Signature Was Prescribed During Model Spin-Up)

Variable	Units	Bern3D	Observational estimates	$\delta^{13}C$ in ‰
Export				
$CaCO_3$	GtC yr^{-1}	0.98	0.72–1.05[a]	
Opal	Tmol Si yr^{-1}	110.02	112[b]	
POC	GtC yr^{-1}	11.93	6.5–13.1[c]	
Deposition				
$CaCO_3$	GtC yr^{-1}	0.49	0.5[d]	2.91
Opal	Tmol Si yr^{-1}	77.6	84[b]	
POC	GtC yr^{-1}	0.65	1.7–3.3[c]	−20.39
Burial				
$CaCO_3$	GtC yr^{-1}	0.22	0.1–0.14[e]	2.88
opal/F_{Si}	Tmol Si yr^{-1}	6.72	9.2[b]	
POC/F_{org}	GtC yr^{-1}	0.24	0.12–0.26[c]	−20.42
F_{ALK}	Gt eq. yr^{-1}	0.41		
F_{DIC}	GtC yr^{-1}	0.46		−9.09
Inventories				
$CaCO_3$ in sediments	GtC	939		3.05
Opal in sediments	Tmol Si	20,658		
POC in sediments	GtC	516		−20.13
Atmospheric CO_2	GtC	589		−6.3
DIC in ocean	GtC	37'157	37,400[f]	0.82
Vegetation and active soils	GtC	2,220	2,000–3,000[g]	−24.3
Input				
F_{CaCO_3}	GtC yr^{-1}	0.14		2.88
F_{CaSiO_3}	Tmol Si yr^{-1}	6.72		
F_{org}	GtC yr^{-1}	0.24		−20.42
$F_{remainder}$	GtC yr^{-1}	0.08		2.88

Note. Values are determined as the mean of the first 100 years after a pre-industrial spin-up in the control run. Corresponding literature estimates are also shown. GtC refers to giga tons of carbon.
[a]Battaglia et al. (2016). [b]Tréguer et al. (2021). [c]Sarmiento and Gruber (2006). [d]Milliman and Droxler (1996). [e]Feely et al. (2004). [f]Key et al. (2004). [g]Ciais et al. (2013).

The burial fluxes of P, Si, ALK, DIC, and $^{13}C_{DIC}$ are diagnosed at the end of the model spin-up and prescribed as the input fluxes for these components (F_P, F_{Si}, F_{ALK}, F_{DIC}, F_{DIC-13}) at the start of transient simulations. $^{13}R_{CaCO_3}$ and $^{13}R_{org}$ are diagnosed from the signatures of the $CaCO_3$ and POC burial. $^{13}R_{remainder}$ is the signature needed to close the ^{13}C budget of the model in equilibrium after the spin-up. All input is assumed to be free of ^{14}C. Equations 3–7 are solved for the steady-state fluxes (F_{org}, F_{CaSiO_3}, F_{CaCO_3}, $F_{remainder}$), and the signature $^{13}R_{remainder}$. To close the isotope budget of the model, $\delta^{13}C$ of $F_{remainder}$ is identical to that of the $CaCO_3$ burial flux (2.88‰, Table 2). This value is around 8‰ higher than typically reported for volcanic CO_2 emissions (Deines, 2002), and implicitly accounts for the fractionation associated with metamorphism and weathering reactions. Table 2 shows steady state fluxes and inventories of $CaCO_3$, POC, and opal, as well as $\delta^{13}C$ signatures. $\delta^{13}C$ of the export flux is not diagnosed in the current model setup. Our model setup is idealized to investigate specifically the impact of changes in $CaCO_3$ weathering and the input of organic material on carbon and its stable isotope. The CO_2 degassing from the lithosphere ($F_{remainder}$), silicate weathering $\left(F_{CaSiO_3}\right)$, and the isotopic signatures of the input fluxes ($^{13}R_{CaCO_3}$, $^{13}R_{org}$, $^{13}R_{remainder}$) are kept constant in all simulations. Further, all input fluxes are diagnosed to

match the simulated burial fluxes at the end of the model spinup, where ocean alkalinity and nutrient inventories, and atmospheric CO_2 are prescribed from modern observations. In Earth's history, CO_2 degassing and weathering of silicate and other rocks varied. These variations in input fluxes caused changes in the carbon inventories of the atmosphere-ocean-land biosphere-sediment system and sedimentary burial rates and governed the long-term evolution of past atmospheric CO_2 and climate by the so-called silicate thermostat (Berner, 1990; Walker et al., 1981).

2.4. Experimental Set-Up and Analysis

The model is spun up over 60 thousand years (Kyr) under 1,765 CE boundary conditions. Atmospheric CO_2 of 277.8 ppm with an isotopic signature of $\delta^{13}C_{atm} = -6.305‰$ and $\Delta^{14}C_{atm} = 0‰$ is prescribed. From the 1,765 CE steady state, at nominal year −100, 100.1 Kyr long experiments are started. After 100 years, that is, in nominal year 0 of the experiments, a total of 16 step-change simulations are started, eighth for F_{CaCO_3} and eighth for F_{org}, covering the range from −80% to +80% in steps of 20%. The corresponding amounts of carbon, ^{13}C, alkalinity, and P (Equations 3–7) are then added to the coastal surface ocean. A subset of the above experiments, namely the changes of +40%, −40%, and the control run, are extended by an additional 500 Kyr simulation period in order for the model to establish new equilibrium after the step-change in carbon isotopes. The wide range of step-changes is chosen to investigate non-linearities in the carbon cycle as further detailed in Section 3.3.

For organic input, an additional 100 Kyr sensitivity simulation is performed to investigate the effect of differences in the $\mathcal{R}_{P:C}$ ratio. We conduct this sensitivity experiment as stoichiometric ratios are fixed in the Bern3D model and do not vary with environmental conditions. However, P is preferentially regenerated from marine sediments under low oxygen conditions (e.g., L. D. Anderson et al., 2001; Delaney, 1998; Ingall & Jahnke, 1994). In the sensitivity experiments, 30% of the P entering marine sediments is immediately dissolved back into the ocean. This P leaching changes the sedimentary and therefore also the input flux $\mathcal{R}_{P:C}$ to about 1:152. Our setup for changing F_{org} is different from a step-change in the ocean P inventory as applied by Tschumi et al. (2011) and others. In the experiments presented in this study, the change in F_{org} implies a sustained change in the input fluxes of P, C, ^{13}C, and ALK. These sensitivity simulations are performed for step-changes of +40% and −40% in F_{org}.

Results presented in this study are relative to a control run to account for any drift over the 600 thousand year (Kyr) simulation period. Generally, drift is small, and amounts, for example, in the case of CO_2, to well below 0.01 ppm Kyr^{-1} in the control simulation. The output frequency for marine 3-D tracer fields after the perturbation is every 10 years during the first 1 Kyr, every 200 years until 10 Kyr, every 1 Kyr until 100 Kyr, and every 5 Kyr thereafter.

Changes in the carbon isotopic fluxes and inventories are expressed in [GtC ‰] by multiplying inventories or fluxes of carbon [GtC] with their corresponding $\delta^{13}C$ signatures [‰]. We attribute the change in the isotopic burial minus input flux to changes (Δ) in carbon burial (B) and input (I) fluxes and in the isotopic signature of the burial flux (δ_B) relative to the equilibrium state after the spin-up (subscript 0) for both POC and $CaCO_3$:

$$\begin{aligned} {}^{13}B - {}^{13}I &= (B_0 + \Delta B) \cdot (\delta_0 + \Delta\delta_B) - (I_0 + \Delta I) \cdot \delta_0 \\ &= \Delta(B - I) \cdot \delta_0 + B_0 \cdot \Delta\delta_B + \Delta B \cdot \Delta\delta_B \end{aligned} \tag{8}$$

Note that the steady state carbon and isotopic burial-input fluxes vanish with $B_0 - I_0 = 0$ and $\delta_{B,0} = \delta_{I,0} = \delta_0$.

2.5. Green's Function Substitute Model

Green's functions for a change in input flux (weathering) are directly obtained from the step-change simulations with Bern3D. Generally, the Green's function can be determined by prescribing a step-like change in forcing (e.g., the magnitude of weathering flux) in a model previously spun up to equilibrium. Then the model is run toward a new equilibrium, and the simulated change $\Delta y(\vec{x}, \tau)$ is monitored for any variable y (e.g., $\delta^{13}C_{DIC}$) for any grid cell, region, or reservoir of interest. The response Δy is normalized by the magnitude of the step-change to yield the Green's function, $r^y(\vec{x}, \tau)$. τ is the time passed since the step-like change and $\vec{x}$ indicates location.

Any forcing history, $F(t)$, may be approximated by a series of small step-like changes, $\Delta F(t_i)$. Then, the response, $\Delta y(\vec{x}, t)$, in variable y at time t and location $\vec{x}$ to this forcing history is for a linear system:

$$\Delta y(\vec{x}, t) = \sum_i \Delta F(t_i) \cdot r^y(\vec{x}, t - t_i). \tag{9}$$

$t - t_i$ represents the time τ_i that has passed since the step-change $\Delta F(t_i)$ at time t_i. The sum is over all step-changes used to approximate the forcing history from its beginning up to time t. The system is assumed in equilibrium at the start of the forcing time series.

Instead of running a complex 3-dimensional dynamic model, its response is approximated by Equation 9, a great efficiency gain. The benefit in comparison to box models is that the internally consistent physical and biogeochemical response of the dynamic model is encapsulated in the Green's function substitute model. A disadvantage of the Green's function approach is that non-linearities in responses to a combination of forcings may be difficult to represent and can lead to substantial differences between results from the original versus the substitute model (Jeltsch-Thömmes et al., 2019). In this study, we restrict the approach to changes in $CaCO_3$ and organic input. For further ease of application, a Green's function can be approximated using Principal Component-Empirical Orthogonal Functions (PC-EOF). The temporal component of the PC-EOF can be approximated by a sum of exponential terms and the substitute model (Equation 9) can be represented by a series of box models and spatial patterns for further computational efficiency (see Jeltsch-Thömmes & Joos, 2020; Joos et al., 2001; Strassmann & Joos, 2018).

The dynamics of a linear system are fully characterized by its Green's function. Although the carbon cycle and the Earth system are not linear, the linear approximation of Equation 9 is often useful. Here, we present Greens's functions for different Earth system components and globally and regionally averaged values for a range of model parameters (cf. Figures 1–6), as well as over a wide range of step changes (−80%–+80% of the unperturbed flux) to evaluate non-linearities (cf. Figures 5c, 5d, and 6). In the discussion in Section 4.2, we will apply Equation 9 for different weathering scenarios, using directly the (normalized) model output from the step simulations described in Section 2.2. To this end, the scaled annual mean time-series responses in CO_2, deep ocean CO_3^{2-}, and mean ocean $\delta^{13}C_{DIC}$ are applied every 1 Kyr. We use the mean of the normalized responses to the +40% and −40% step-change in the input of $CaCO_3$ and organic matter, respectively. We further apply the normalized responses to the +40% and −40% step-change individually to generate lower and upper uncertainty bounds for emulator results.

3. Results

3.1. Earth System Response to a 40% Increase in the $CaCO_3$ Weathering Input Flux

We first address Earth system responses to changes in $CaCO_3$ weathering. A key finding is that changes in $CaCO_3$ weathering cause a shift in the isotopic fractionation during marine photosynthesis, in response to altered CO_2, and significant changes in $\delta^{13}C$ of the atmosphere, ocean, and land biosphere. The prescribed 40% step-like increase in the $CaCO_3$ weathering flux translates into an increase in the inputs of carbon and alkalinity in a 1:2 M ratio (Figures 1a and 1b). The $\delta^{13}C$ signature of the total carbon input is also increased by 1.3‰ (Figure 1c) because the relative share of the isotopically heavy $CaCO_3$ weathering input becomes larger. The individual $\delta^{13}C$ signatures of the $CaCO_3$ and organic input remain unchanged in our setup.

In response to the step-increase in carbon and alkalinity (ALK) input, a new equilibrium of the climate-carbon system is approached with an e-folding timescale (τ) of about 10 thousand years (Kyr, Figures 1d–1l, and 2a). In other words, concentrations and fluxes typically change most rapidly immediately after the step and then slowly approach a new equilibrium following roughly an exponential curve. As a remarkable exception, $\delta^{13}C$ isotopic signatures continue to change over a few 100 thousand years (Figure 1m). Possible fits of the responses in ΔCO_2 and $\Delta\delta^{13}C_{DIC}$ are provided as equations in Figure 1.

Atmospheric CO_2 decreases, by almost 32 ppm (Figure 1d), as the surface ocean concentration of ALK increases about twice as much as that of DIC (Figures 1f and 1g). Surface air temperature (SAT) decreases by about 0.5°C (Figure 1e) in response to lower atmospheric CO_2. Ocean circulation changes remain small, and the Atlantic meridional overturning circulation (AMOC) stabilizes ~0.5 Sv (3%) below the initial state (not shown). DIC and ALK increase by about 37 and 68 mmol m^{-3} on ocean average (Figures 1f and 1g). Due to this "ocean alkalinization," ocean pH, and carbonate ion concentration increase in the surface and deep ocean, and the calcium carbonate saturation horizon deepens on average by about 700 m in the North Pacific (Figures 1h–1j). In turn, marine biogenic $CaCO_3$ is better preserved in ocean sediments, and the net transfer of $CaCO_3$ from the ocean to the sediments, and eventually the lithosphere, increases by about 25% (Figure 1l). The equilibrium increase in $CaCO_3$ burial of 25% corresponds to the implied increase in the Ca^{2+} input of 25% in our scenario which results from constant F_{CaSiO_3} and a 40% increase in F_{CaCO_3}. The modeled carbonate saturation horizon in

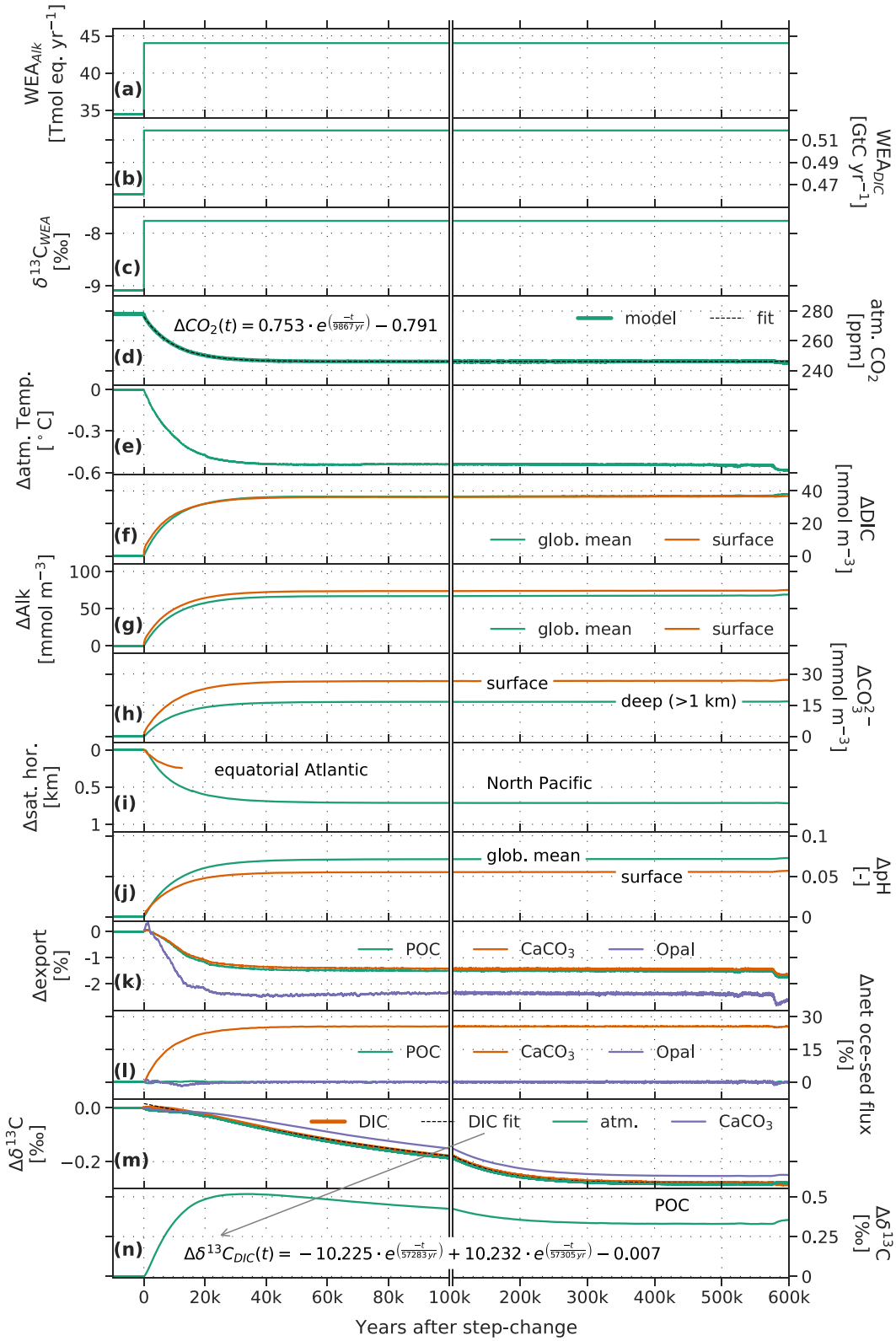

Figure 1. Timeseries evolution of the forcing (a–c) and a set of Earth system properties (d–n) simulated with Bern3D for a 40% step increase in the $CaCO_3$ input flux. For better visibility, data in panels (e, k, l, and m) (only $CaCO_3$) are shown as 100 yr running means. Surface refers to upper 100 m. Note that the fits given in the figure refer to a +1% change in $CaCO_3$ input.

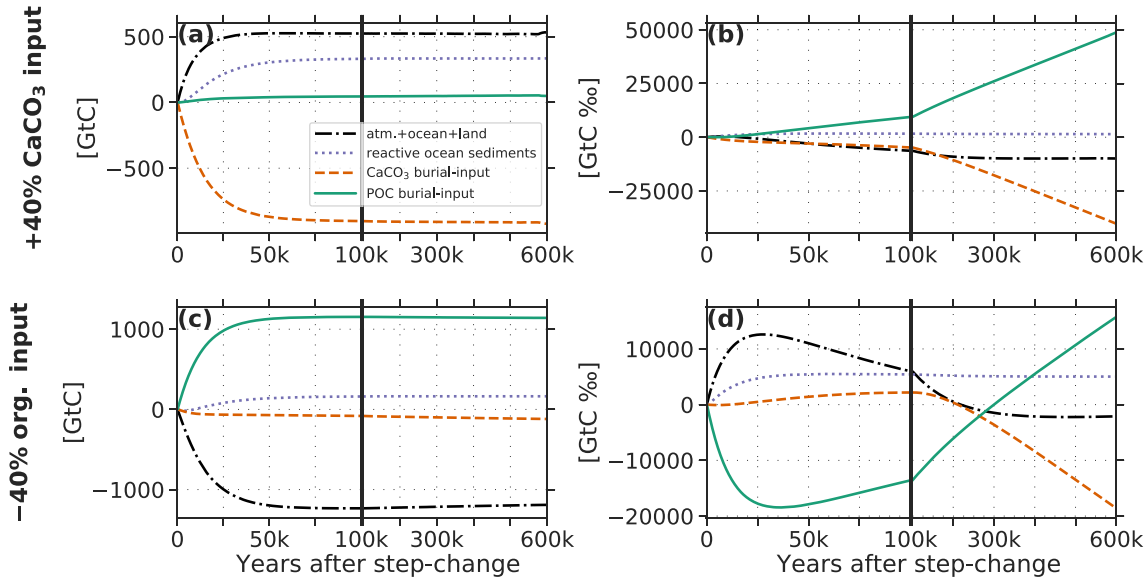

Figure 2. Carbon (a), (c) and carbon isotopic (b), (d) budget for step-changes of +40% in the $CaCO_3$ (a), (b) and −40% in the organic (c), (d) input flux. The changes in the inventories of the atmosphere plus ocean plus land biosphere (black dash-dotted line) and reactive ocean sediments (purple dotted line) are compared to cumulative input-burial imbalances for $CaCO_3$ (orange dashed line) and POC (green solid line). The anomalies in the inventory of the atmosphere, ocean, land biosphere, and reactive sediments equal the cumulative input-burial imbalances at any time.

the equatorial Atlantic was already relatively close to the ocean bottom before the step-change in input, leaving little room for further deepening (Figure 1i). The timescale of this carbonate compensation process (~8–10 Kyr, e.g., Archer et al., 1997, 1998; Jeltsch-Thömmes & Joos, 2020) is reflected in the timescale of the CO_2 perturbation of ~10 Kyr.

Changes in global export fluxes of POC, $CaCO_3$, and opal are comparably small (<3%, Figure 1k) and result in only small declines in the sedimentary POC and opal inventories (Figure 1l). Export production generally decreases as a result of lower temperatures and increased sea-ice area, with the largest changes in the Southern Ocean. The higher input of ALK to the surface ocean (Figure 1a), together with the slight reduction in $CaCO_3$ export (Figure 1k), causes a larger increase of ALK in the surface than the deep ocean (Figure 1g), while the surface-to-deep gradient in DIC remains almost unaffected by the increase in $CaCO_3$ weathering (Figure 1f).

We establish budgets for the carbon (Figure 2a) and alkalinity perturbations by comparing accumulated burial-input imbalances for $CaCO_3$ and POC with changes in the major reservoirs, atmosphere, ocean, and sediments. Carbon and ALK fluxes are stoichiometrically linked. C:ALK molar ratios of 1:2 and 117:−17 are applied for $CaCO_3$ and POC and the molar weight of carbon is 12.01 g mol^{-1}. Carbon and alkalinity storage in the ocean increases by about 600 GtC and 91 Petamol eq, respectively. The majority of the perturbation in the combined atmosphere-ocean system (~521 GtC; 91 Pmol eq) and the reactive ocean sediments (~334 GtC; 60 Petamol eq) is driven by imbalances in the $CaCO_3$ burial-input flux (~−912 GtC; 152 Petamol eq). Contributions from imbalances associated with the POC cycle are small (~53 GtC; −0.6 Petamol eq) (Figure 2a). Accordingly, the majority of change in the reactive ocean sediments is explained by an increased $CaCO_3$ content (~361 GtC; 60 Petamol eq) with little contribution from decreased POC storage (~−27 GtC; 0.3 Petamol eq). The values refer to means over the period 500–550 Kyr after the step-change.

3.1.1. Carbon Isotopes

After an initial small increase, resulting from the higher $\delta^{13}C$ signature of the weathering input after the step-change (Figure 1c), $\delta^{13}C$ decreases gradually after the step in the atmosphere, ocean, land biosphere (AOB), and sedimentary $CaCO_3$ reservoirs. $\delta^{13}C$ in these reservoirs stabilizes at about −0.28‰ lower values after several hundred Kyr (Figure 1m). In contrast, $\delta^{13}C$ of sedimentary POC increases relatively fast to peak at around 30 Kyr after the step. Afterward, the anomaly decreases slightly to stabilize at about 0.35‰ after several hundred Kyr (Figure 1n).

Generally, the majority of the carbon isotopic perturbation following a step-change in $CaCO_3$ weathering can be attributed to a shift in the fractionation factor during marine photosynthesis. Lower atmospheric CO_2 (Figure 1d) and therefore lower surface water $[CO_{2,aq}]$ reduces fractionation during marine photosynthesis (see Table 1). As a result, $\delta^{13}C$ of the POC export flux increases, and the mean $\delta^{13}C$ of sedimentary POC peaks about 30 Kyr after the step-change in $CaCO_3$ input (Figure 1n). Consequently, $\delta^{13}C$ of the POC burial flux increases, and ^{13}C is removed by POC burial-input. This removal causes $\delta^{13}C$ of DIC to decrease (Figures 1m and 2b). The negative perturbation in $\delta^{13}C_{DIC}$ is incorporated into newly formed $CaCO_3$ and POC, explaining the gradual decrease in $\delta^{13}C$ of the $CaCO_3$ sediment inventory (Figure 1m) and burial flux, and the post-peak decrease in the $\delta^{13}C$ signature of the POC sediment inventory (Figure 1n).

The $\delta^{13}C$ perturbation budget is shown in (Figure 2b). The accumulated isotopic perturbation in the AOB system stabilizes at ∼−9,800 GtC‰ after several hundred kyr (Figure 2b, black line). The change is mainly linked to the decrease in the mean isotopic signature of the constituents of the AOB system (Figure 1m); The contribution from the change in the carbon inventory of the AOB system is small (not shown). The perturbation in reactive sediments accumulates to ∼+1,500 GtC ‰(Figure 2b, purple dotted). This positive perturbation is mainly due to the decrease in the sedimentary POC inventory, with further contributions from the change in POC signature and from $CaCO_3$.

The equilibration of $\delta^{13}C$ after the change in $CaCO_3$ input is controlled by burial-input imbalances in both the $CaCO_3$ and POC cycles (Figure 2b). This is different than for carbon for which burial-input imbalances of $CaCO_3$ dominate the response (Figure 2a). The $\delta^{13}C$ perturbation in the AOBS system is stabilized by the canceling effects of POC versus $CaCO_3$ burial-input flux. More ^{13}C atoms are removed by POC burial than added by the organic input. Taken the fluxes together, ^{13}C is removed from the AOBS system by the so-called POC burial-input flux (green line in Figure 2b). On the other hand, the $CaCO_3$ burial-input flux adds ^{13}C atoms to the AOBS system (Figure 2b, orange line).

For further understanding, we attribute the net isotopic fluxes of POC and $CaCO_3$ burial-input according to Equation 8 (Figures 3a–3c). The three terms considered are linked to changes in the net burial-input carbon flux ($\Delta(B-I)\cdot\delta_0$), in the $\delta^{13}C$ signature of the burial flux ($\Delta\delta_B\cdot B_0$), and the perturbations in the burial carbon flux and signature ($\Delta B\cdot\Delta\,\delta_B$) (Figure 3). The majority of the carbon isotopic perturbation in response to a 40% increase in $CaCO_3$ input is caused through changes in the $\delta^{13}C$ signatures of the POC and $CaCO_3$ burial fluxes (Figure 3b). Changes in the carbon isotopic budget due to the carbon burial-input imbalance (Δ(B-I) δ_0) are comparably small (Figure 3a). They are larger for $CaCO_3$ than for POC as a result of the larger cumulative change in the burial-input flux for $CaCO_3$ than for POC (Figure 2a). For the same reason, the contribution of $\Delta B\cdot\Delta\delta_B$ is substantially larger for $CaCO_3$ (∼8,000 GtC‰) than POC (∼0 GtC‰) (Figure 3c).

The perturbation in $\delta^{13}C_{DIC}$ varies spatially within the ocean. The surface-to-thermocline gradient in $\delta^{13}C_{DIC}$ is reduced after the step in $CaCO_3$ input. In Figure 5a horizontally averaged $\Delta\delta^{13}C_{DIC}$ is plotted versus time and depth. $\Delta\delta^{13}C_{DIC}$ is on average slightly less negative in the thermocline than in surface and deep ocean waters. The differences of $\Delta\delta^{13}C_{DIC}$ in surface versus $\Delta\delta^{13}C_{DIC}$ of thermocline and deep waters are small, <0.05‰ on average (Figure 5c). They are a consequence of reduced fractionation during marine photosynthesis resulting from lower $[CO_{2,aq}]$. Thus, the POC flux transports a less negative isotopic signal from the surface to the thermocline, where most of the POC is remineralized. Changes in circulation could contribute to a different $\delta^{13}C_{DIC}$ gradient but variations in modeled ideal age of water masses are very small (<10 years, not shown). The response to a 40% decrease in $CaCO_3$ input yields a very similar response but with inverse sign (Figures 5b and 5c) and is not further discussed here.

In summary, the carbon-climate system equilibrates typically within a few tens of Kyr after the step-change in $CaCO_3$ input, whereas it takes several hundred Kyr to establish a new equilibrium for $\delta^{13}C$ signatures. Changes in proxy-related variables are a decrease in CO_2 and Surface air temperature (SAT), an increase in carbonate ion concentration with deepening of the lysocline and higher carbonate preservation, near absent or small responses in POC and opal bulk fluxes, and a long-term decrease in $\delta^{13}C$ of atmospheric CO_2 and DIC with a slightly reduced surface-to-thermocline gradient in $\delta^{13}C_{DIC}$.

Remarkably, changes in $CaCO_3$ input cause changes in $\delta^{13}C$ of DIC and atmospheric CO_2 of several tenths of a permil. Such $\delta^{13}C$ changes are comparable to reconstructed changes over glacial–interglacial cycles. Also remarkable, the change in $\delta^{13}C$ of $CaCO_3$ and DIC is with −0.2‰ opposite to the change in the signature of the input flux of +1.3‰. This is different to expectations of equal change in $\delta^{13}C$ signatures when treating the

climate system as one box (e.g., Equation 1 in Schrag et al. (2013)) and neglecting changes in fractionation. The contribution of the POC cycle, in particular a smaller isotopic fractionation during marine photosynthesis under lower CO_2, is key to understanding the isotopic changes. These $\delta^{13}C$ changes become only evident when considering the reorganization of the carbon cycle within the climate system instead of treating the climate system as a single reservoir and when considering POC input and burial fluxes in addition to $CaCO_3$ input-burial imbalances.

3.2. Earth System Response to a 40% Decrease in the Organic Input Flux

A 40% decrease in the organic input flux reduces P and carbon inputs, increases the alkalinity input, and leads to an enrichment in the $\delta^{13}C$ signature of the total carbon input (Figures 4a–4d). Similar as for the change in $CaCO_3$ input, most carbon cycle fluxes and tracers adjust after the step-change toward a new equilibrium on time scales of order ∼7.5 Kyr (Figures 4e–4m). Exceptions are the $CaCO_3$ ocean-to-sediment flux which is only temporarily perturbed (Figure 4m, orange lines), and $\delta^{13}C$ signatures which show changes over several hundred Kyr (Figures 4n and 4o). The e-folding timescale for the fit of the atmospheric CO_2 perturbation is different from the $CaCO_3$ step-change experiment, as the underlying processes differ. While in the case of the $CaCO_3$ step-change experiment, $CaCO_3$ compensation is the controlling process, in the case of the organic step-change, an interplay between changes in POC export production and burial rates, mediated by changes in the phosphorous inventory are at play, as described in detail below.

In response to the step-reduction in carbon input, DIC, atmospheric CO_2, and temperature (Figures 4e–4g), as well as AMOC decrease. The magnitude is similar to the changes shown in Section 3.1. In the steady state solution of the model, the organic input flux contributes about half of the carbon input (Table 2). Modeled changes in the atmospheric and marine carbon inventory are thus a direct result of reduced carbon input after the step-change.

The marine P inventory decreases as a result of the reduced P input, limiting biological productivity. Production and export of organic material, as well as of $CaCO_3$, decreases by about 23% (Figure 4l). In turn, the POC flux to sediments and eventually POC burial decreases by 40%, thereby exactly offsetting the reduction in organic matter input at the new equilibrium. Opal export is only reduced by a couple of percents. At the end of the simulation, opal export is reduced in high latitudes as a result of increased sea-ice cover, and increased in low- and mid-latitudes (not shown).

In response to reduced DIC, the carbonate ion concentration increases as (CO_3^{2-}) ∼ [ALK]-[DIC]) (Figures 4g–4i). ALK input and ALK in the ocean changes only little during the first 10 Kyr (Figures 4b and 4h). The shift to a higher (CO_3^{2-})/[DIC] ratio goes hand in hand with an increase in pH (Figure 4k). The increase in (CO_3^{2-}) causes a deepening of the saturation horizon by about 800 m in the North Pacific (in the equatorial Atlantic the saturation was already relatively close to the ocean bottom before the step-change in input, leaving little room for further deepening Figure 4j). In turn, more $CaCO_3$ is transferred from the ocean to the sediments in the first 50 Kyr after the step-change (Figure 4m), despite the ∼23% reduction in $CaCO_3$ export. This $CaCO_3$ transfer lowers the ocean's ALK inventory (Figure 4h), and the temporary perturbation in the $CaCO_3$ flux to sediments vanishes again (Figure 4m).

These marine carbon cycle changes affect the surface-to-deep ocean gradients in DIC and ALK (Figures 4g and 4h; orange vs. green line). The decrease in DIC and ALK is larger in the deep ocean than in the surface, and the surface-to-deep gradient in DIC is reduced on global average. These changes in gradients are linked to the reduction in POC and $CaCO_3$ export, that tend to remove less carbon and slightly less alkalinity from the surface ocean.

Altogether, the AOB reservoir loses ∼1,196 GtC (Figure 2c). This change is driven by a cumulative burial-input imbalance in the POC cycle of ∼1,142 GtC with little contribution from the $CaCO_3$ cycle (∼−115 GtC) (Figure 2c). The overall increase in carbon storage in reactive ocean sediments (163 GtC) is explained by a gain of $CaCO_3$ (∼367 GtC) which is partly balanced by a loss of POC (∼−203 GtC). Again, values refer to means over the period 500–550 Kyr after the step-change.

3.2.1. Carbon Isotopes

Similar to the response to changing $CaCO_3$ input, a shift in the isotopic fraction during marine photosynthesis is important for the long-term evolution of $\delta^{13}C$. Less input of isotopically light organic carbon shifts the $\delta^{13}C$ signature of the atmosphere and ocean to higher values at first. Similarly, the $\delta^{13}C$ signature of the net ocean-sediment flux of carbon increases. After peaking at around 20 Kyr, $\delta^{13}C$ in the atmosphere and ocean, as

well as $\delta^{13}C$ of sedimentary POC and $CaCO_3$ (and therefore also the burial flux) decrease slowly to reach new steady-state values after several 100 Kyr (Figures 4n and 4o).

The driving processes of these changes take place on roughly two timescales (Figures 2d, 3d–3f). The timescales are caused by the different response times in the carbon ($\Delta(I - B)$) and carbon isotopic budgets. The carbon cycle approaches a new equilibrium after multiple millennia and can be seen as constant after roughly 50 Kyr (Figure 2c). The positive cumulative imbalance in the isotopically light POC burial-input (Figure 2c, solid green line) leads to a reduced removal of ^{13}C from the reactive carbon pools (Figure 2d, solid green line). This causes the initial increase in $\delta^{13}C$ in these reservoirs (Figures 4n, 4o, 2d, and 3d). This initial, shorter timescale, is reflected in the fit of the $\delta^{13}C_{DIC}$ perturbation for the first 30 Kyr after the step-change (equation in panel n, Figure 4).

In contrast, lower atmospheric CO_2 and therefore lower $[CO_{2,aq}]$ lead to less fractionation during marine photosynthesis and an increase in $\delta^{13}C$ of sedimentary POC (Figure 4o) and the POC burial flux. Hereby, isotopically heavy carbon ^{13}C is continuously removed from the combined AOB carbon pool (Figures 2d and 3e). On timescales of multiple 10 Kyrs, the change in signature outweighs the effect of the increased cumulative burial-input flux on the carbon isotopic budget and the direction of change in $\delta^{13}C$ signatures is reverted (Figures 4n, 4o, and 2d). The longer timescale of this second phase of the $\delta^{13}C_{DIC}$ perturbation is reflected in the fit for $t > 30$ Kyr (panel o, Figure 4).

$\delta^{13}C$ of $CaCO_3$ follows surface ocean $\delta^{13}C_{DIC}$. The associated isotopic flux (Figures 2d and 3e, dashed orange lines) eventually balances the effect of the POC cycle ((Figures 2d, 3d–3f), green lines) on the carbon isotopic budget, leading to stable $\delta^{13}C$ in the AOB system after 300 Kyr (Figures 2d and 4n).

The perturbation in the POC export causes a strong perturbation in the surface-to-deep gradient of $\delta^{13}C_{DIC}$. Figure 5e shows the horizontally averaged evolution of the perturbation in $\delta^{13}C_{DIC}$ after the step-like decrease in input of organic material. Both, the reduction in the export of POC by about 23% (Figure 4m, green line) and the increase of its $\delta^{13}C$ signature (Figure 4o) weaken the overall surface-to-thermocline and the surface-to-deep gradient in $\delta^{13}C_{DIC}$. Changes in the export of labile dissolved organic matter may also somewhat contribute. Further, changes in input minus burial fluxes also affect spatial isotopic gradients. A clear perturbation in the gradient between the euphotic zone (uppermost two vertical layers in the model) and the underlying waters develops, leading to strongly enriched $\delta^{13}C_{DIC}$ perturbation in thermocline and intermediate depth waters, even reaching down to the ocean floor, as compared to the surface (see dark red blob in Figure 5e). After about 200 Kyr a vertical perturbation pattern with a negative $\delta^{13}C_{DIC}$ perturbation in the surface, a slightly positive $\delta^{13}C_{DIC}$ perturbation in the thermocline and intermediate depth waters, and a slightly negative $\delta^{13}C_{DIC}$ perturbation in waters below ~2 km depth has developed and appears to prevail. The surface-to-thermocline gradient is changed by ~0.25‰ and the surface-to-deep gradient by ~0.15‰ on global average (Figure 5f).

In the case of a 40% increase in organic material input, the spatio-temporal evolution of $\Delta\delta^{13}C_{DIC}$ is generally comparable, however the absolute perturbation in global mean $\delta^{13}C_{DIC}$ is initially smaller and stabilizes at higher levels, and changes in the surface-thermocline and surface-deep gradients are smaller. First, the change in the overall $\delta^{13}C$ signature of weathering carbon input does not change by the same absolute amount for an increase and decrease in organic input. A 40% decrease in organic input changes the overall $\delta^{13}C$ signature of weathering carbon input by ~2‰, while a 40% increase changes it by ~3‰. The initial perturbation in $\delta^{13}C_{DIC}$ caused by the changed input is thus smaller for an increase than a decrease (cf. Figures 5d–5f). Second, while for a 40% decrease in organic input, the POC export flux is reduced by about ~23%, in the case of a 40% increase the POC export flux increases by only ~13%, thus affecting surface-thermocline and surface-deep gradients differently. This non-linearity in the carbon isotopic response has to be kept in mind, when interpreting proxy records in light of these step-change experiments.

3.2.2. Sensitivity Experiment for Sedimentary P Leaching

Next, we turn to the results from the sensitivity experiment with idealized higher phosphate leaching from sediments (dashed lines in Figure 4). 30% of the P in organic matter leaving the ocean is immediately "leached back" to the water column. In this model setup, the steady-state input flux of P is reduced in comparison to the standard run (Figure 4a, solid vs. dashed line).

Generally, the response to a reduction in the organic input flux is amplified in the case of the sensitivity experiment. In particular, the reduction in atmospheric CO_2 is 30% larger than in the standard model setup, as are the peak perturbations in $\delta^{13}C$ of DIC and CO_2 around 20 Kyr. The 40% reduction in the organic input flux translates

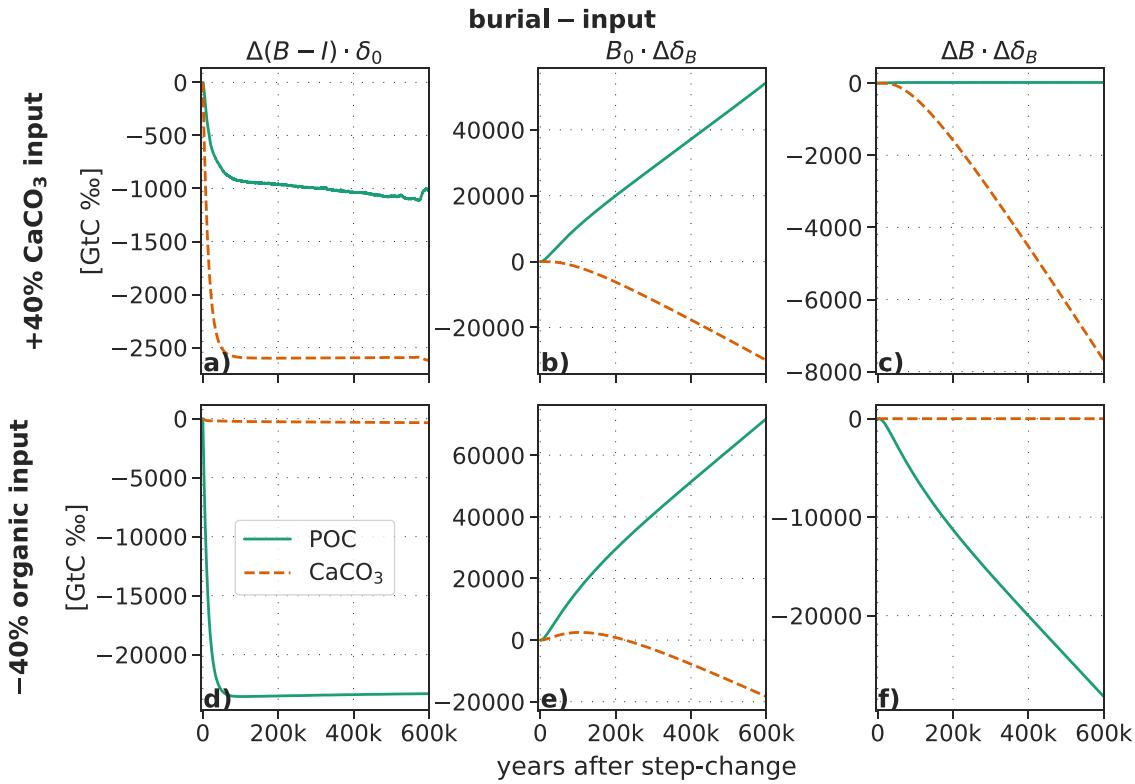

Figure 3. Cumulative contribution of the burial-input flux to the carbon isotopic perturbation for a (a, b, c) 40% increase in the $CaCO_3$ and a (d, e, f) 40% decrease in the organic input flux. The contribution is split into changes in the (a), (d) carbon flux ($\delta_0 \cdot \Delta F$), the (b), (e) $\delta^{13}C$ signature ($\Delta\delta \cdot F_0$) of the flux, and their (c), (f) combination ($\Delta\delta \cdot \Delta F$).

into a smaller absolute change in input in the sensitivity compared to the standard run, because the steady-state input flux of P is smaller (Figure 4a). In turn, P limitation for marine biological production is less severe in the sensitivity experiment. This results in slightly less reduced export fluxes of organic matter and $CaCO_3$, as compared to the standard run (Figure 4l), translating into temporarily higher net ocean-sediment loss fluxes (Figure 4m; dashed vs. solid lines). The higher loss of POC and $CaCO_3$ causes DIC (and to a lesser extent ALK) and CO_2 to decrease more in the sensitivity than standard setup.

Differences in the isotopic perturbation can be readily understood from differences in the burial-input fluxes and an even further reduced fractionation during marine photosynthesis owing to the lower CO_2 concentration (see Table 1 and Figures 4e, 4m, and 4o). The majority of the carbon isotopic perturbation is again driven by the POC cycle (cf. Figures 2c and 2d). The burial-input imbalance in the POC cycle is larger in the sensitivity experiment with preferential phosphate leaching from sediments, as compared to the standard organic input step-change experiment. This leads to an amplified increase in the $\delta^{13}C$ signature of the reactive carbon pools (see the larger perturbation in $\delta^{13}C$ in Figures 4n and 4o). At the same time, lower atmospheric CO_2 and thus lower $[CO_{2,aq}]$ lead to less fractionation during marine photosynthesis and an increase in $\delta^{13}C$ of the POC burial flux. In total, this leads to initially higher positive $\delta^{13}C$ values in the atmosphere and ocean for the sensitivity experiment with subsequent declines in differences (Figures 4n, 6b, and 6d).

3.3. Scalability of Step-Change Responses

Here, we address the linearity of responses in carbon and carbon isotopes to step-changes of different magnitudes (Figure 6). In a linear system, the responses shown in Figures 1 and 4 would be independent of the magnitude of the step-change. Then, the impact of any evolution of changes in $CaCO_3$ or organic matter input could be exactly described with the help of the responses or Green's functions shown in Figures 1 and 4. While the carbon cycle is known to be non-linear, near-linear behavior may still emerge within certain limits of change. In Figure 6 we compare the responses in CO_2, DIC, and their $\delta^{13}C$ signatures from eight step-change simulations where $CaCO_3$ or organic matter input was changed at nominal time $t = 0$ over a wide range (−80%–+80%). All responses are

10.1029/2022PA004577

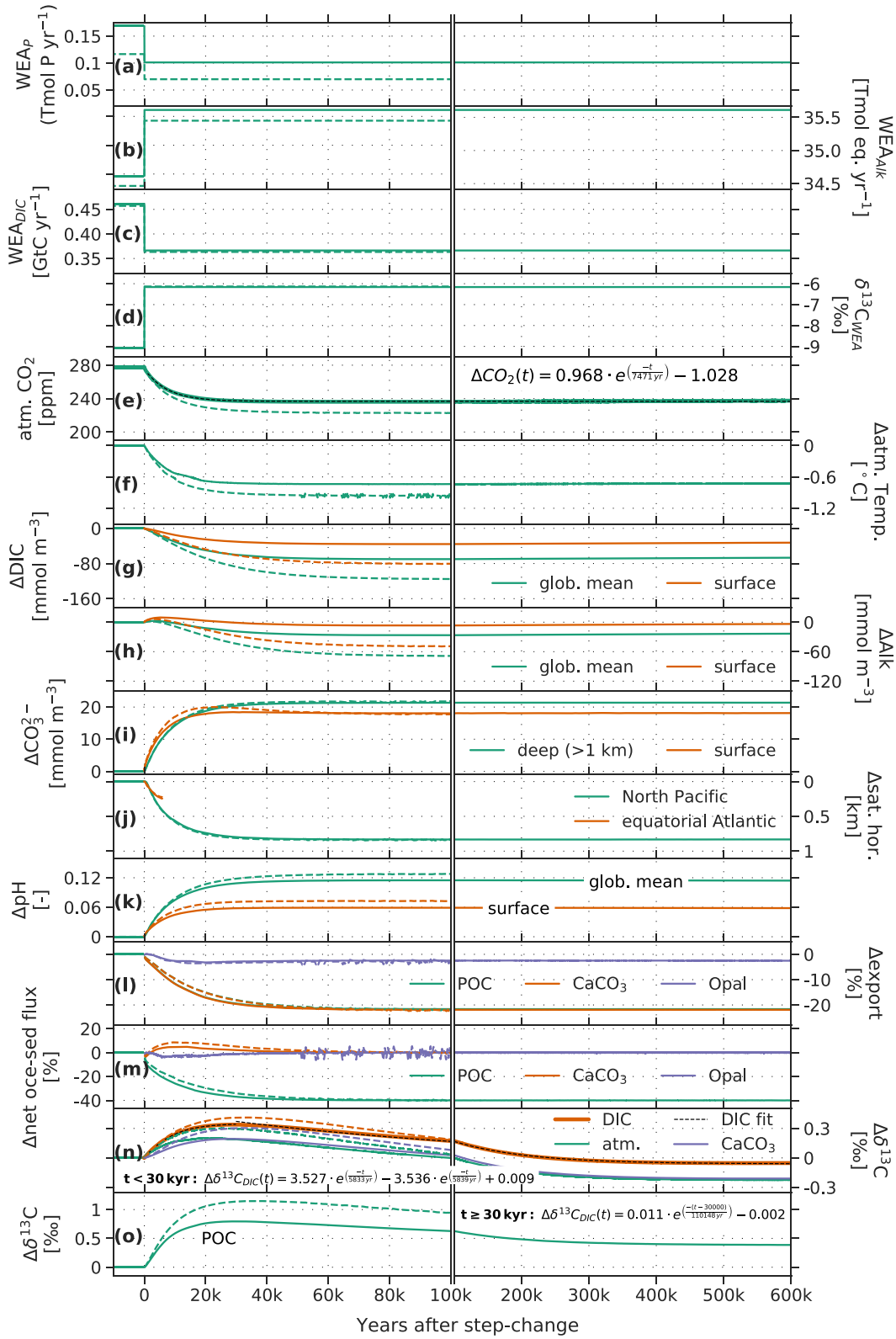

Figure 4. Timeseries evolution of the forcing (a–d) and a set of Earth system properties (e–o) simulated with Bern3D for a 40% decrease in the organic input flux. Dashed colored lines show results from the sensitivity experiment with a sedimentary C:P ratio of ~152:1. For better visibility, data in panels (f, l, m, and n) (only $CaCO_3$) is shown as 100 yr running means. Surface refers to upper 100 m. The green line for POC is hidden by the orange line for $CaCO_3$ in panel (l). Note that the fits given in the figure refer to a −1% change in organic input.

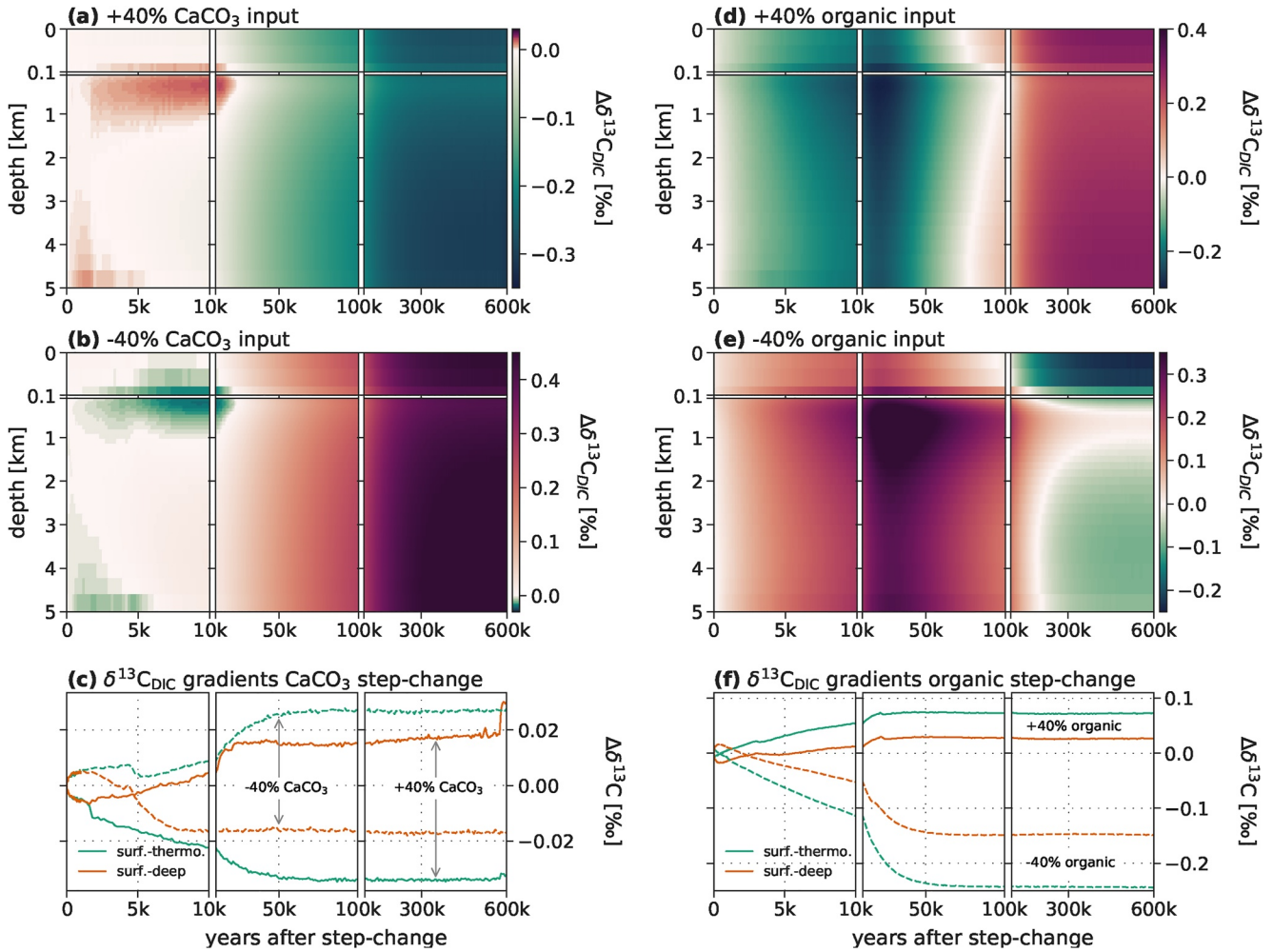

Figure 5. Hovmoeller-type diagram of the $\delta^{13}C_{DIC}$ perturbation for step-changes of (a), (d) +40% in the $CaCO_3$ and organic input fluxes, (b), (e) −40% in the $CaCO_3$ and organic input fluxes, and (c), (f) timeseries of the surface (euphotic zone)-to-thermocline (~600–700 m) and surface-to-deep (2.5–3.5 km) gradient for the respective simulations with the Bern3D model.

normalized to a step increase in $CaCO_3$ or decrease in organic matter input of 40% for comparison with the experiments discussed above. The responses for steps within ±40% are visually highlighted and linked by blue (for $CaCO_3$) and red (for organic matter) shading. The responses for larger step-changes are not further discussed.

Generally, linearity is higher for step-changes in the $CaCO_3$ input as compared to organic matter input. Changes in DIC, $\delta^{13}C_{atm}$, and $\delta^{13}C_{DIC}$ are near-linear in the case of step-changes in $CaCO_3$ input, although non-linearities increase somewhat with time by up to ±14–16% relative to the overall change at 100 Kyr (Figures 6b–6d). The largest uncertainties are associated with the response in CO_2, where the mean response is −39 ppm, with a spread of ±7 ppm (±18%) after 100 Kyr and the range between +40% and −40% $CaCO_3$ input. The response in CO_2 is larger for a reduction than an increase in $CaCO_3$ input of equal magnitude (Figure 6a). In case of the other variables, the spread after 100 Kyr is ±4% for DIC, ±16% for $\delta^{13}C_{atm}$, and ±16% for $\delta^{13}C_{DIC}$. For step-changes in the organic input, near linearity is found for changes in DIC (spread: ±7%) and, to a lesser extent, for atmospheric CO_2 (±7 ppm, ±14%), $\delta^{13}C_{atm}$ (±20% relative to peak change), while the spread covers 0.2‰ (±37% relative to peak change) for $\delta^{13}C_{DIC}$ after 100 Kyr and the range between +40% and −40% organic matter input.

In summary, the assumption of a near-linear response appears reasonable for changes in organic matter and $CaCO_3$ input within ±40% around the mean state. Thus, the response functions displayed in Figures 1 and 4 broadly characterize the response to changes in $CaCO_3$ and organic matter input, enabling the construction of a simple emulator to simulate responses to time-varying input in a cost-efficient and transparent way as done in Section 4.2.

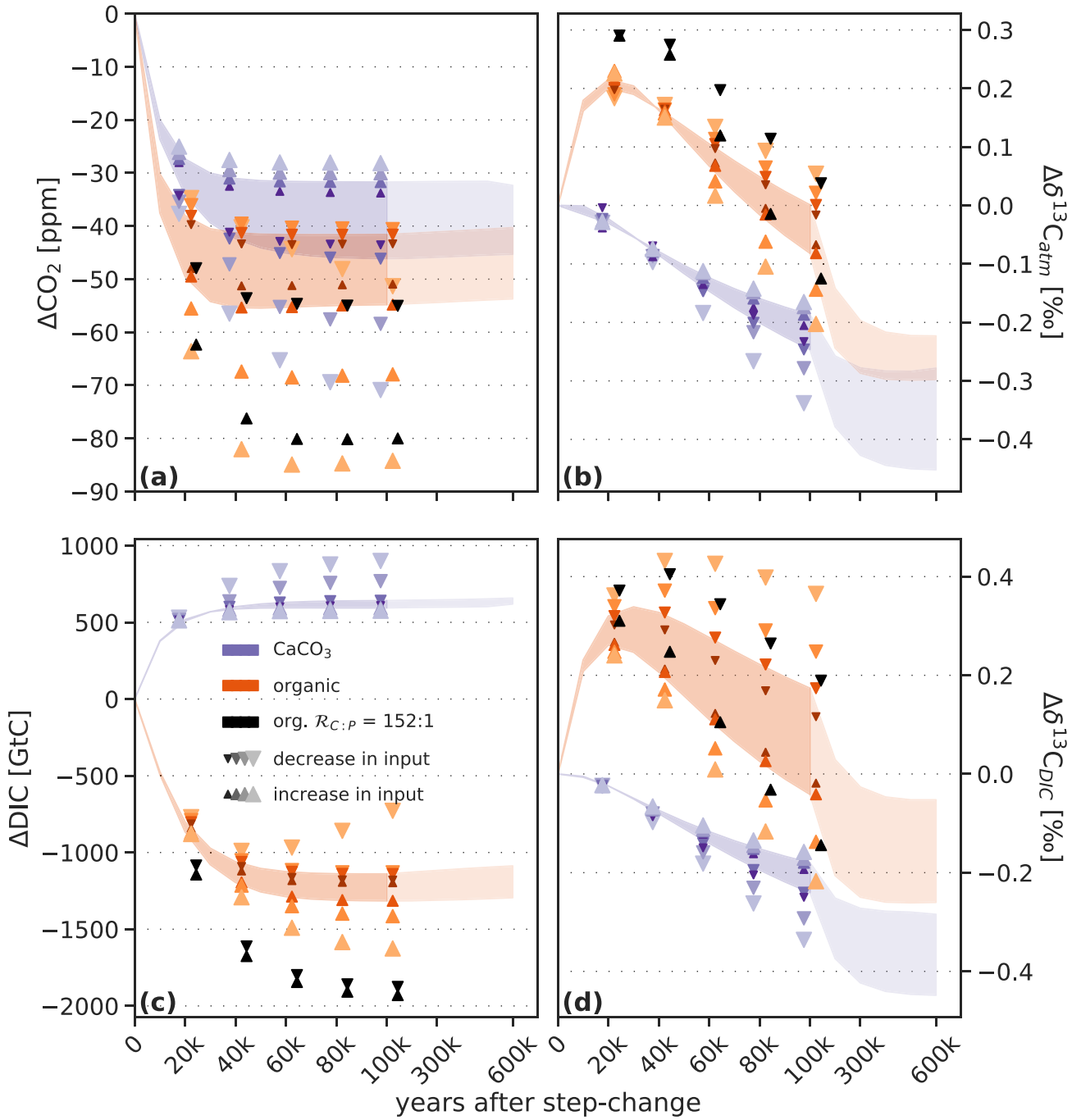

Figure 6. Normalized response functions. Change in (a) CO_2, (b) $\delta^{13}C_{atm}$, (c) dissolved inorganic carbon, and (d) $\delta^{13}C_{DIC}$ to step-changes in the input of $CaCO_3$ (blue), organic material (red), and organic material with a different C:P ratio (black, see Section 2.2). Step-changes range from −80% to 80% in 20% increments (size of the markers). Results are scaled to an increase of 40% in the case of $CaCO_3$ and a decrease of 40% in the case of organic material. Shadings indicate the range from the +40% to −40% step in input. Triangles are slightly offset in *x*-direction for visibility and black triangles show results only for an in-/decrease of 40% in the organic input flux.

4. Discussion

State-of-the-art Earth System Models or Earth System Models of Intermediate Complexity that explicitly represent processes on a 3-dimensional spatial grid and sub-annual time scales are computationally too expensive for simulations exceeding millions of years. However, the characteristic spatio-temporal responses of such complex models may be used to build cost-efficient substitute models (Section 2.3) that account for the underlying spatio-temporal complexity of the involved processes. In the future, such models may also include spatially

explicit weathering or ice sheets. The Green's response functions from the Bern3D Earth System Model of Intermediate Complexity for changes in the net input of organic matter and $CaCO_3$ may also be viewed as a first step toward bringing spatial scales to modeling the carbon cycle over periods of many millions of years. In such long simulations, the AOB, and interactive sediments are usually taken as single reservoirs which differs from our approach, as we here explicitly consider the transfer of carbon, alkalinity, and phosphorus between these reservoirs and within the ocean. Further, future work may expand the scope of this study by investigating Green's responses for variations in $CaSiO_3$ weathering and associated climate feedbacks using spatially resolved models.

The response timescales and amplitudes to perturbations in the input from the lithosphere are governed by the interplay between ocean circulation and air-sea exchange, nutrient transport to the ocean surface, marine biological productivity and the export of biogenic particles, and remineralization and redissolution of biogenic particles within the water column and sediments. Spatial gradients within the ocean and ocean sediments are important. For example, the removal rate of $\delta^{13}C$ perturbations is significantly modified by $\delta^{13}C$ gradients within the ocean, influencing the isotopic composition of the burial flux of organic and $CaCO_3$ particles in the lithosphere (Jeltsch-Thömmes & Joos, 2020). Further, the development of spatio-temporal gradients in response to changes in weathering input could be important to consider in the interpretation of palaeo-records, as the perturbation might look very different, depending on ocean depth (cf. Figure 5).

The long timescales and the spatial complexity associated with burial-input imbalances and the carbon cycle is a challenge when investigating the glacial–interglacial variations of the past few million years. Box models may not fully resolve spatial gradients, whereas glacial–interglacial simulations are computationally too expensive with weathering-sediment-enabled Earth System Models (Lacroix et al., 2020) and are even demanding for Earth System Models of Intermediate Complexity (e.g., Colbourn et al., 2013; Ganopolski & Brovkin, 2017; Menviel et al., 2012; Willeit et al., 2022). Cost-efficient substitute models, representing faithfully the response of spatially resolved models, provide an alternative.

In brief, evaluating the response to a step-like change reveals underlying system dynamics and spatio-temporal response characteristics. This is useful for model-model comparison and for understanding the model responses to a perturbation. Further, the response can be used to build a cost-efficient substitute model (or emulator) to explore different forcing histories over long time scales (see Section 4.2).

4.1. Uncertainties and Limitations

We apply an Earth system model of intermediate complexity. The use of the Bern3D model enables us to conduct 600 Kyr long simulations considering fluid dynamics, biogeochemical processes, and marine sedimentation in a spatially resolved 3-dimensional setting. This is a progress compared to box models or 2-dimensional ocean models, typically applied for such long time scales. However, many processes are still represented by simplified parameterizations and some of these, as, for example, the dissolution rate constants in the marine sediments or the remineralization of organic matter in the water column, rely on global uniform parameter choices.

Another limitation relates to the stoichiometric ratios used in the model. The question of the C:P ratio in marine sediments and preferential P leaching to the ocean is discussed in the literature (e.g., L. D. Anderson et al., 2001; Delaney, 1998; Ingall & Jahnke, 1994). Under low oxygen conditions, for example, P is preferentially regenerated from marine sediments, (e.g., Ingall & Jahnke, 1994). This could lead to a positive feedback loop where more P is brought to the ocean surface enhancing primary production and organic matter export, and, in turn, enhancing organic matter transport to and remineralization at depth, further depleting bottom water oxygen through consumption of oxygen during remineralization (e.g., Kemena et al., 2019; Niemeyer et al., 2016; Palastanga et al., 2011; Van Cappellen & Ingall, 1994; Wallmann, 2010; Watson, 2016). Release of additional P from sediments could have a strong impact on $\delta^{13}C$ (see e.g., Tschumi et al., 2011, for a step-increase in the ocean's P inventory). In the current setup of the Bern3D model, we assume constant Redfield ratios in the ocean and sediment. Further, in the standard step-change experiment of the organic input flux, the same constant C:P ratio of 117:1 is applied. To address this limitation, we conducted an additional experiment, where 30% of the P entering marine sediments in the model is immediately released back to the ocean (see Section 2.1). While the quantitative results differ, the qualitative response is similar for the experiment with and without this idealized enhanced P leaching. Model formulations could be revised in the future for varying C:P ratios, preferential P leakage from sediments under low oxygen concentrations as done in the HAMOCC and UVic models (e.g., Kemena et al., 2019; Niemeyer et al., 2016; Palastanga et al., 2011), and variable stoichiometric ratios for biological production, for

example, Matsumoto et al. (2020). Lacroix et al. (2020) further discuss the question of C:P ratios of riverine weathering input of organic material. While terrestrial dissolved organic matter exhibits very high C:P ratios of up to 2583:1 (Compton et al., 2000; Meybeck, 1982), the ratio is uncertain in POM, with a range of 56–499 (Compton et al., 2000; Meybeck, 1982; Ramirez & Rose, 1992). In the experiments here, weathering of terrestrial dissolved organic material is not considered and the input flux F_{org} is assumed to originate from previously buried organic matter. In line with Lacroix et al. (2020), the C:P ratio of this F_{org} flux from the litosphere is the same as of oceanic POM.

For the evolution of $\delta^{13}C$, the organic matter cycle and fractionation during marine photosynthesis play an important role. Here, this fractionation is described using the empirical relationship with dissolved CO_2 by Freeman and Hayes (1992). Additionally, there are other environmental factors besides dissolved CO_2 that might affect fractionation during marine photosynthesis (Goericke & Fry, 1994). Jahn et al. (2015) implemented three parameterizations in their ocean model. One where fractionation varies with dissolved CO_2 and two also considering phytoplankton growth rates. Overall, all three parameterizations lead to the expected pattern of high $\delta^{13}C_{DIC}$ in surface waters and low $\delta^{13}C_{DIC}$ values in water that has been out of contact with the atmosphere for a long time. Liu et al. (2021) found good $\delta^{13}C$ data-model agreement for discrimination varying with dissolved CO_2 according to Popp et al. (1989), while the agreement was less favorable with a parameterization additionally varying with local phytoplankton growth rates (Laws et al., 1995). These findings lend indirect justification for applying the parameterization of Freeman and Hayes (1992), which is similar to that of Popp et al. (1989). While the application of alternative parameterizations would somewhat affect the quantitative findings of this study, the main messages would likely remain unchanged. A shift in the isotopic fractionation during photosynthesis due to altered dissolved CO_2 would change the isotopic signature of the burial flux and the evolution of $\delta^{13}C$ in the ocean-atmosphere-land biosphere-sediment system.

Finally, another uncertainty regarding the evolution of the $\delta^{13}C$ perturbation is related to the use of the simple 4-box representation of the land biosphere with constant fractionation. This simplification is expected to have a minor impact on multi-millennial timescales as the land biosphere stores only around 5% of the carbon in the combined atmosphere-ocean-land biosphere-sediment system.

4.2. Scenarios for the Past 800,000 Years: Application of the Green's Function Substitute Model

We apply the Green's function emulator (Equation 9; Section 2.3) to easily investigate different scenarios for changes in $CaCO_3$ weathering and organic matter input over the past 800,000 years. We use the normalized responses to the +40 and −40% step-change in input for $CaCO_3$ and organic matter. Uncertainty ranges and best estimates are computed by using the normalized responses to the +40% and −40% step-change in input for $CaCO_3$ and organic matter and the average of both responses, respectively. This emulator is an approximation and non-linear interactions with carbon cycle changes other than those related to changes in weathering input are not taken into account. The aim of this exercise is not to provide conclusive answers how past changes in input fluxes affected atmospheric CO_2 and the carbon cycle, but rather to illustrate the usefulness of the Green's function approach to explore different scenarios and hypotheses.

In the first scenario, we apply the 0-dimensional version of the RokGeM v0.9 model (Colbourn et al., 2013) where $CaCO_3$ input is a function of atmospheric CO_2 (Bereiter et al., 2015) and global mean SAT. SAT evolution is computed by linearly scaling the Antarctic temperature reconstruction of Jouzel et al. (2007), assuming a difference in SAT between preindustrial (PI) and Last Glacial Maximum (LGM) of 5.5 K, at the lower end of estimates reported by Tierney et al. (2020). RokGeM yields $CaCO_3$ weathering to be about 40% lower at LGM than PI (Figure 7, turquoise). This is in contrast to Börker et al. (2020) who suggest $CaCO_3$ weathering to be about 30% higher at LGM than PI. In our second scenario, we linearly scale the $\delta^{18}O$ record of Lisiecki and Raymo (2005) to yield an LGM-PI difference of +30% in $CaCO_3$ input.

The scenario based on Börker et al. (2020) yields LGM minima of up to ∼15 ppm lower than at PI. In contrast, the scenario based on RokGem yields up to more than 20 ppm higher CO_2 during glacials (Figures 7a and 7b). Overall, differences between the two literature-based scenarios are up to 35 ppm or about a third of the glacial–interglacial CO_2 amplitude. Similarly, changes in global mean deep ocean (>1 km) CO_3^{2-} are opposite and differences between the two scenarios are up to 18 mmol m^{-3}. Generally, CO_2 and CO_3^{2-} follow changes in weathering without much delay and capture some multi-millennial features of the forcing, while $\delta^{13}C_{DIC}$ shows a strongly smoothed signal. Variations in $\delta^{13}C_{DIC}$ are on the order <0.05‰ (for reference, the PI-LGM difference amounts

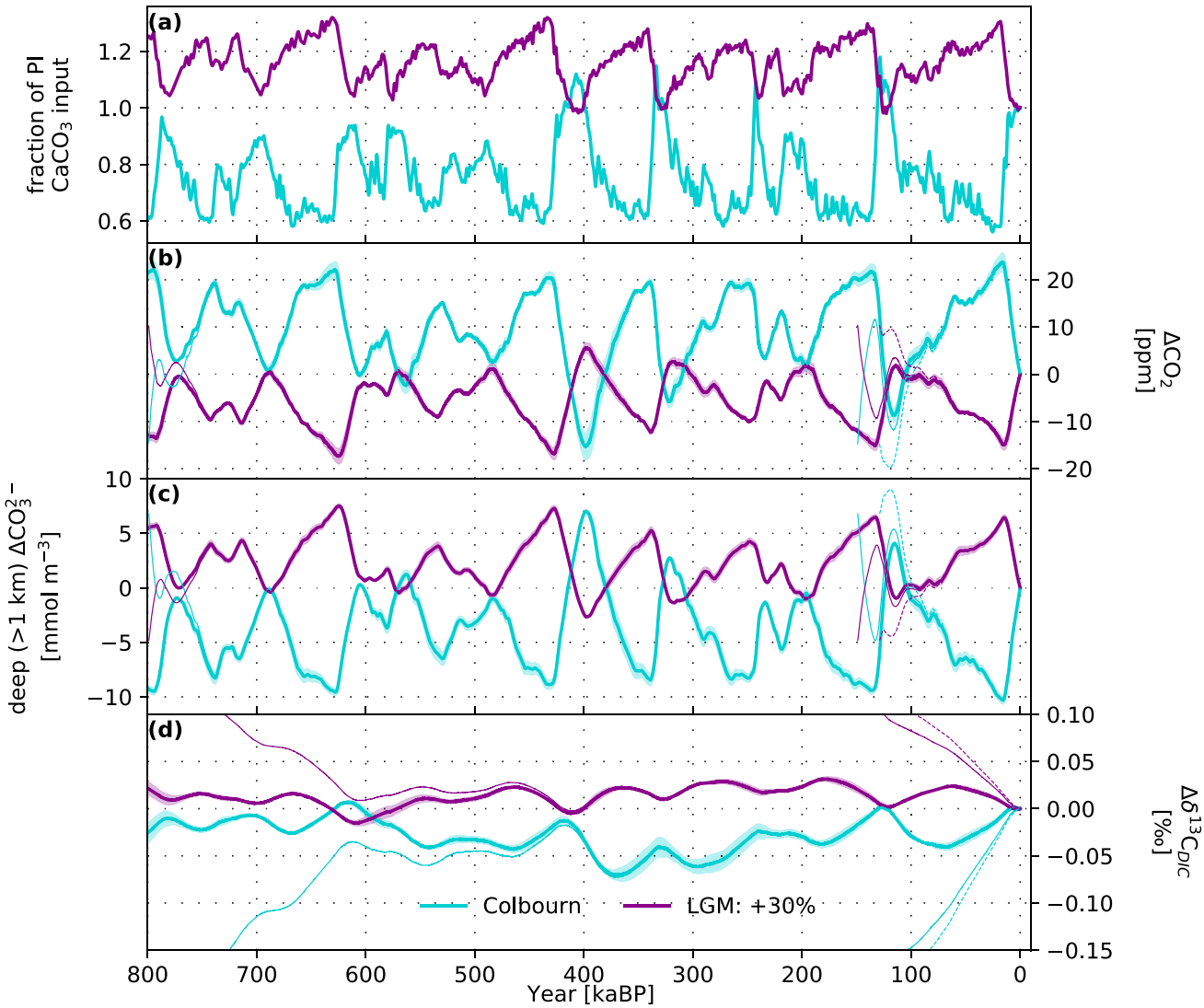

Figure 7. Two contrasting literature-based $CaCO_3$ weathering scenarios. (a) Prescribed changes in $CaCO_3$ weathering input (magenta: +30% in Last Glacial Maximum (LGM), based on reconstructions of $CaCO_3$ weathering by Börker et al. (2020) and scaled with $\delta^{18}O$ (Lisiecki & Raymo, 2005); Turquoise: as calculated with the Rock Geochemical Model RokGeM v0.9 (Colbourn et al., 2013), where maximum LGM cooling of 5.5 K is scaled with the Antarctic temperature reconstruction by Jouzel et al. (2007)). Changes (relative to PI) in (b) atmospheric CO_2, (c) deep ocean (>1 km) CO_3^{2-}, and (d) global mean $\delta^{13}C_{DIC}$ as emulated using the responses of the step-change experiment. The first glacial cycle was repeated twice before starting the standard run at 800 Kyr (thick lines). Upper and lower uncertainty bounds (shading) and best estimates (lines) are computed by using the normalized responses to the +40 and −40% step-change in input for $CaCO_3$ and organic matter and the average of both responses, respectively. Sensitivity simulations, illustrating the drift associated with a "cold start," were started directly at 800 (thin solid lines), 150 (thin solid lines), and 130 kaBP (thin dashed lines); results show that initial conditions affect simulated CO_2 for several ten thousand years and $\delta^{13}C$ for several hundred thousand years.

to 0.34 ± 0.19‰, C. D. Peterson et al. (2014)) and the timing of maxima/minima does not directly mirror changes in the forcing (Figure 7d).

In the third scenario, we adopt the "shelf-weathering" hypothesis by Wallmann et al. (2016), where input of organic-derived material to the ocean is elevated during periods of low sea level. Taking their PI-LGM change in POC weathering at face value (see panel (h), Figure 3 in Wallmann et al., 2016) translates into a ∼10% change of the total organic input in the Bern3D model. This PI-LGM difference in forcing is then scaled with $\delta^{18}O$ (Lisiecki & Raymo, 2005) to yield a forcing history of the past 800 Kyr (Figure 8a). This yields CO_2 changes of up to ∼10 ppm with higher CO_2 during glacials than interglacials (Figure 8b). Changes in $\delta^{13}C_{DIC}$ are on the order of 0.05‰ with lower values during glacials. This means that about 15% of the observed PI-LGM $\delta^{13}C_{DIC}$ change (C. D. Peterson et al., 2014) could be attributed to changes in input from shelves. Contrary to changes in the

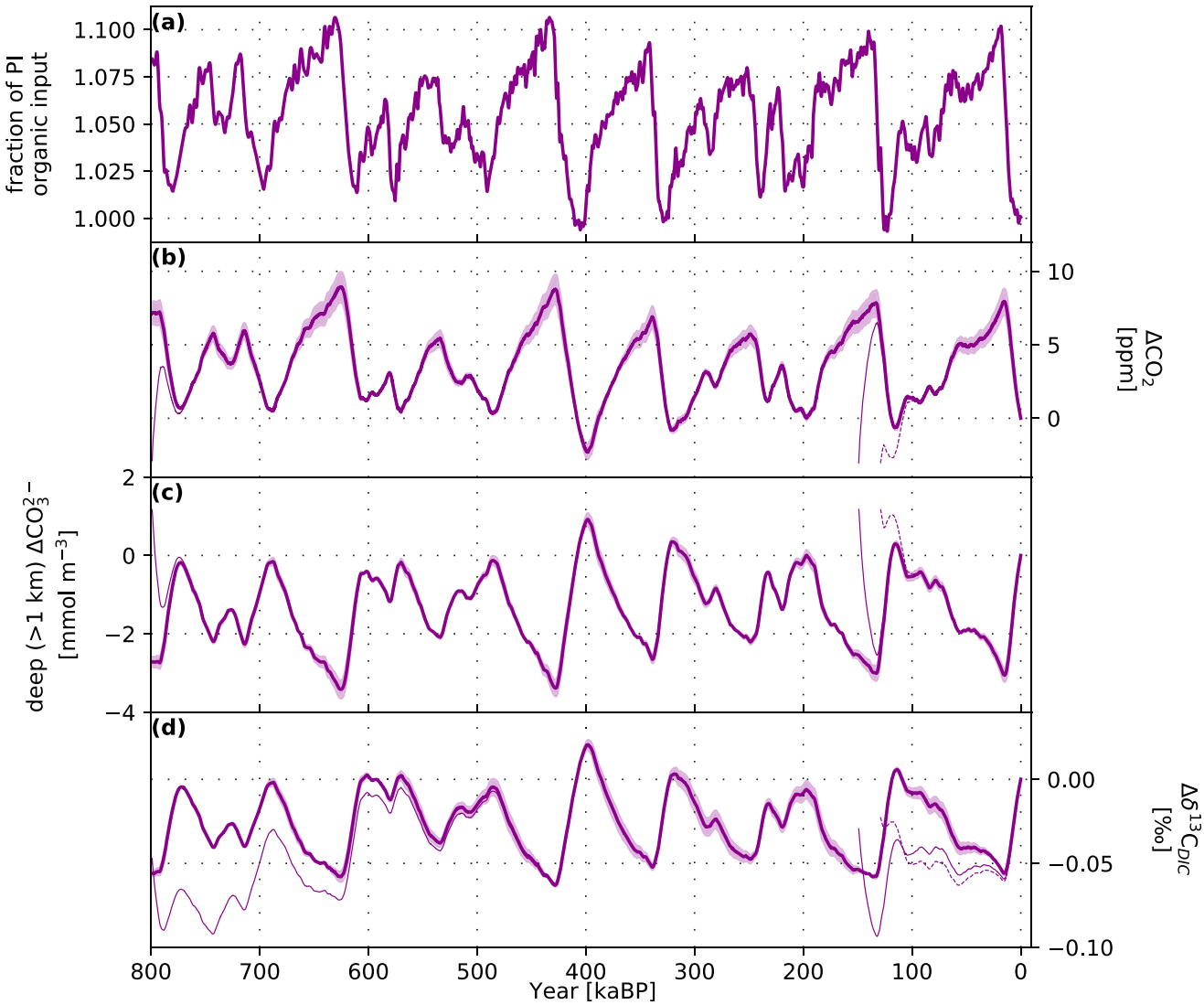

Figure 8. As Figure 7 but for a scenario with varying input of organic-derived material (P:C:ALK = 1:117:−17 and $\delta^{13}C = -20.42$ ‰), based on Wallmann (2014) and Wallmann et al. (2016).

$CaCO_3$ weathering, the signal in $\Delta\delta^{13}C_{DIC}$ is less smoothed and the timing reflects the forcing history (Figures 8a and 8d). This is likely a results from the initial strong perturbation in $\delta^{13}C_{DIC}$ resulting from changes in the input $\delta^{13}C$ signature (see Figures 3n, 5d–5f and Section 3.2).

Multi-proxy evidence suggests that glacial–interglacial CO_2 variations are driven by different carbon cycle processes, with partly offsetting impacts on $\delta^{13}C$ and other proxies (Jeltsch-Thömmes et al., 2019). Hypotheses invoking changes in weathering or coral reef growth (Berger, 1978) to explain low glacial atmospheric CO_2 imply an open-system ocean increase in alkalinity and CO_3^{2-} (cf. Figures 1g and 1h), and a deeper lysocline (Figure 1i) compared to interglacial conditions. However, observational evidence suggests small glacial–interglacial changes in the lysocline depth and CO_3^{2-} concentrations (Yu et al., 2014). Changes in alkalinity in response to weathering or coral reef growth changes cannot be the sole driver of glacial–interglacial CO_2 change. Yet, these processes, as well as changes in the input of organic material, should not be neglected for explaining glacial–interglacial CO_2 and proxy change, as these processes likely contributed to the overall variations.

Finally, we address how well the emulator captures the Bern3D response. To this end, three additional 100 Kyr long test simulations were performed where $CaCO_3$, organic, and $CaCO_3$ and organic input fluxes were varied (see Supporting Information S1). Generally, the emulator faithfully reproduces results from the Bern3D model.

The root mean square differences between the emulator and Bern3D are <5% of the simulated amplitude in atmospheric CO_2, and deep ocean (>1 km) $CaCO_3^{2-}$ and $\delta^{13}C_{DIC}$; the difference is larger (15%) when comparing it to the small $\delta^{13}C_{DIC}$ signal under varying $CaCO_3$ input, but still small in absolute terms with a root mean square difference of 0.001 ‰ only (see Figure S1 and Table S1 in Supporting Information S1). Differences between results from a substitute model and its parent model may become larger when combining several forcings. For example, Jeltsch-Thömmes et al. (2019), combining seven forcings in Bern3D and a substitute, find differences in the amplitude of deglacial change of less than 10% for $\delta^{13}C$ of atmospheric CO_2 and DIC and almost 30% for atmospheric CO_2.

4.3. How to Initialize Earth System Models: The Glacial-Interglacial Cold Start Problem

The long adjustment timescales of carbon and $\delta^{13}C$ to perturbations in input-burial imbalances pose a serious challenge for model initialization. Initial conditions affect the evolution of CO_2 and $\delta^{13}C$ over several ten thousand and hundred thousand years, respectively. In the standard setup of the emulator, the forcing history of the first glacial cycle is repeated twice, before starting the simulation at the nominal year 800 kaBP. We illustrate the impact and potential biases of such a "cold start" (Hasselmann et al., 1993) by starting the emulator at 800 kaBP, the beginning of our scenarios, at 150 kaBP, that is, close to glacial maximum conditions, and at 130 kaBP, near the beginning of the last interglacial.

The initial trends in CO_2 and CO_3^{2-} deviate strongly from standard results during many millennia (thin vs. thick lines in Figure 7) for all three sensitivity runs. This initial drift obscures the signals found in the standard run. For $\delta^{13}C$, deviations extend as expected over several hundred thousand years. Results for $\delta^{13}C$ of the simulations started at 150 and 130 kaBP are useless and highly misleading. The simulated change in $\delta^{13}C_{DIC}$ over the last glacial–interglacial cycle is about four times larger in the runs started at 150 and 130 kaBP than the variations in the standard run.

The initial adjustment after a cold start is an intrinsic property of the Earth system as implemented in the parent Bern3D model (see Figures 1 and 4) and inherited by the emulator. The results highlight that models used to simulate the last deglacial or glacial–interglacial cycles and featuring input and burial fluxes must be carefully initialized to avoid wrong results and interpretations.

5. Conclusions

We conducted idealized, 600-Kyr-long simulations following a step-change in the input fluxes of DIC, ALK, P, and $\delta^{13}C$ from the lithosphere to the ocean. The purpose is to investigate response timescales and underlying processes. To this end, we assumed changes in a conceptual input flux releasing the elements of isotopically depleted, former organic matter (F_{org}; P:ALK:DIC = 1:−17:−117 with $\delta^{13}C = -20.42‰$) or from $CaCO_3$ weathering (F_{CaCO_3}; ALK:DIC = 2:1 with $\delta^{13}C = 2.88‰$).

A remarkable result is the differences in the response timescales for atmospheric CO_2 and climate versus that of the stable carbon isotope ratio, $\delta^{13}C$. Equilibrium is approached after a few ten thousand years for CO_2 and climate but only after a few hundred thousand years for $\delta^{13}C$ in the atmosphere, land biosphere, ocean, and reactive sediments (Figures 1 and 4). For CO_2, and similar for climate and other carbon-cycle parameters such as DIC, alkalinity, CO_3^{2-}, pH, saturation horizon, export production, and sedimentary burial fluxes, an e-folding adjustment occurs with a timescale of ∼7,500 years for the step in F_{org} and ∼9,900 years for the step in F_{CaCO_3}. For $\delta^{13}C$, a long-term e-folding adjustment occurs with a timescale of ∼110,000 years for the step in F_{org} and ∼60,000 years for the step in F_{CaCO_3}.

The process chain for establishing a new isotopic equilibrium is similar for both perturbations. Isotopic fractionation during marine photosynthesis is diminished due to lower dissolved CO_2 in the surface ocean. This causes an increase in $\delta^{13}C$ of newly formed organic matter. In turn, a larger burial of ^{13}C is mediated by organic matter burial. This larger ^{13}C burial, in concert with smaller photosynthetic fractionation, causes $\delta^{13}C$ of DIC and newly formed $CaCO_3$ to decrease. In turn, a larger burial of ^{13}C is mediated by $CaCO_3$ burial which compensates for the reduced ^{13}C burial by organic matter at the new equilibrium.

The compensating role of organic matter and $CaCO_3$ burial highlights that both cycles must be considered when interpreting glacial-interglacial or longer-term changes recorded in the $\delta^{13}C$ proxy records. The often-held view

that changes in the $CaCO_3$ cycle do not substantially impact $\delta^{13}C$, because isotopic signatures are similar for $CaCO_3$ and DIC, is not viable on multi-millennial timescales. Similarly, the neglect of organic matter cycling in sediment-burial models causes biases.

Ocean processes should ideally be represented in a spatially resolved model setting when simulating $\delta^{13}C$ variations. The process chain governing the adjustment of $\delta^{13}C$ causes spatial gradients of $\delta^{13}C$ and other tracers within the ocean. For example, the change in the organic matter input-burial balance substantially changes the surface-to-deep $\delta^{13}C$ gradient. Similarly, circulation and biogeochemical changes under orbital forcing are expected to have distinct spatial imprints with implications for the sediment burial-nutrient feedback (Roth et al., 2014; Tschumi et al., 2011).

The application of a step-change in input allows for probing the so-called Green's function response. The normalized responses are used to build a simple, cost-efficient emulator of the spatially resolved, dynamic model. Simulating 1 million years takes a few seconds with the emulator, while it would take about 3 months using Bern3D. The emulator is applied in a range of literature-based scenarios for the past 800,000 years to estimate carbon cycle changes to plausible time-varying input fluxes from the lithosphere or shelves. These reveal differences in simulated CO_2 of up to a third of the reconstructed glacial–interglacial amplitude, and differences in CO_3^{2-}, and small (0.05–0.1 ‰), but non-negligible, changes in $\delta^{13}C$. Our emulator is probably most useful for periods with a close-to-modern continental configuration. However, Green's function emulators could also be valuable for studying Earth's long history.

The long adjustment time scales of ten thousand years, and even a hundred thousand years for $\delta^{13}C$, pose a serious challenge for sediment-enabled model simulations. The model needs to be initialized carefully to avoid model drift obscuring the responses to any applied forcing, rendering results misleading and useless, as exemplified in cold-start simulations with the emulator.

Our results highlight the importance to consider weathering–burial (input–output) imbalances and interactions between the atmosphere-ocean-land biosphere system and reactive ocean sediments in modeling studies that investigate CO_2 and $\delta^{13}C$ on multi-millennial and longer timescales. A thorough understanding of the mechanisms affecting atmospheric CO_2, $\delta^{13}C_{DIC}$, CO_3^{2-} and other carbon cycle parameters will help in the interpretation of paleo-records. Already small imbalances in the burial-input cycle can have large effects on carbon and carbon isotopes in the Earth system and are thus likely candidates to have contributed to the reconstructed glacial–interglacial variations.

Acknowledgments
The authors acknowledge funding from the Swiss National Science Foundation (No. 200020_200511) and the European Union's Horizon 2020 research and innovation program under Grant agreement No 820989 (project COMFORT, Our common future ocean in the Earth system-quantifying coupled cycles of carbon, oxygen, and nutrients for determining and achieving safe operating spaces with respect to tipping points). The work reflects only the authors' view; the European Commission and their executive agency are not responsible for any use that may be made of the information the work contains. We thank Markus Adloff and Fabrice Lacroix for fruitful discussions and comments on the work. Valuable and constructive feedback by D. Archer, M. Hain, and one anonymous reviewer, as well as during the editorial handling by M. Huber, is thankfully acknowledged and further helped to improve the manuscript. Some of the calculations were performed on UBELIX, the high-performance computing cluster at the University of Bern. We further thank G. Jansen for technical support. Open access funding provided by Universitat Bern.

Conflict of Interest

The authors declare no conflicts of interest relevant to this study.

Data Availability Statement

Data used for the figures and necessary for construction of the emulator are available at Jeltsch-Thömmes and Joos (2023).

References

Anderson, L. A., & Sarmiento, J. L. (1994). Redfield ratios of remineralization determined by nutrient data analysis. *Global Biogeochemical Cycles*, *8*(1), 65–80. https://doi.org/10.1029/93GB03318

Anderson, L. D., Delaney, M. L., & Faul, K. L. (2001). Carbon to phosphorus ratios in sediments: Implications for nutrient cycling. *Global Biogeochemical Cycles*, *15*(1), 65–79. https://doi.org/10.1029/2000GB001270

Archer, D., Kheshgi, H., & Maier-Reimer, E. (1997). Multiple timescales for neutralization of fossil fuel CO_2. *Geophysical Research Letters*, *24*(4), 405–408. https://doi.org/10.1029/97GL00168

Archer, D., Kheshgi, H., & Maier-Reimer, E. (1998). Dynamics of fossil fuel CO_2 neutralization by marine $CaCO_3$. *Global Biogeochemical Cycles*, *12*(2), 259–276. https://doi.org/10.1029/98GB00744

Archer, D., & Maier-Reimer, E. (1994). Effect of deep-sea sedimentary calcite preservation on atmospheric CO_2 concentration. *Nature*, *367*(6460), 260–263. https://doi.org/10.1038/367260a0

Archer, D., Winguth, A., Lea, D., & Mahowald, N. (2000). What caused the glacial/interglacial atmospheric pCO_2 cycles? *Reviews of Geophysics*, *38*(2), 159–189. https://doi.org/10.1029/1999rg000066

Archer, D., Winguth, A., Pierrehumbert, R., Broecker, W., Tobis, M., & Jacob, R. (2000). Atmospheric pCO_2: Sensitivity to the biological pump in the ocean. *Global Biogeochemical Cycles*, *14*(4), 1219–1230. https://doi.org/10.1029/1999gb001216

Bastiaansen, R., Dijkstra, H. A., & Heydt, A. S. V. D. (2021). Projections of the transient state-dependency of climate feedbacks. *Geophysical Research Letters*, *48*(20), e2021GL094670. https://doi.org/10.1029/2021GL094670

Battaglia, G., Steinacher, M., & Joos, F. (2016). A probabilistic assessment of calcium carbonate export and dissolution in the modern ocean. *Biogeosciences*, *13*(9), 2823–2848. https://doi.org/10.5194/bg-13-2823-2016

Bereiter, B., Eggleston, S., Schmitt, J., Nehrbass-Ahles, C., Stocker, T. F., Fischer, H., et al. (2015). Revision of the EPICA Dome C CO_2 record from 800 to 600 Kyr before present. *Geophysical Research Letters*, *42*(2), 542–549. https://doi.org/10.1002/2014GL061957

Berger, A. (1978). Long-term variations of daily insolation and quaternary climatic. *Changes*, *35*(12), 2362–2367. https://doi.org/10.1175/1520-0469(1978)035⟨2362:LTVODI⟩2.0.CO;2

Bergman, N., Lenton, T., & Watson, A. (2004). COPSE: A new model of biogeochemical cycling over Phanerozoic time. *American Journal of Science*, *304*(5), 397–437. https://doi.org/10.2475/ajs.304.5.397

Berner, R. A. (1990). Atmospheric carbon dioxide levels over Phanerozoic time. *Science*, *249*(4975), 1382–1386. https://doi.org/10.1126/science.249.4975.1382

Berner, R. A. (2006). GEOCARBSULF: A combined model for Phanerozoic atmospheric O_2 and CO_2. *Geochimica et Cosmochimica Acta*, *70*(23), 5653–5664. (A Special Issue Dedicated to Robert A. Berner). https://doi.org/10.1016/j.gca.2005.11.032

Börker, J., Hartmann, J., Amann, T., Romero-Mujalli, G., Moosdorf, N., & Jenkins, C. (2020). Chemical weathering of loess and its contribution to global alkalinity fluxes to the coastal zone during the last glacial maximum, mid-holocene, and present. *Geochemistry, Geophysics, Geosystems*, *21*(7), e2020GC008922. https://doi.org/10.1029/2020GC008922

Broecker, W. S. (1970). A boundary condition on the evolution of atmospheric oxygen. *Journal of Geophysical Research (1896-1977)*, *75*(18), 3553–3557. https://doi.org/10.1029/JC075i018p03553

Broecker, W. S., & Peng, T.-H. (1987). The role of $CaCO_3$ compensation in the glacial to interglacial atmospheric CO_2 change. *Global Biogeochemical Cycles*, *1*(1), 15–29. https://doi.org/10.1029/GB001i001p00015

Broecker, W. S., & Peng, T.-H. (1989). The cause of the glacial to interglacial atmospheric CO_2 change: A polar alkalinity hypothesis. *Global Biogeochemical Cycles*, *3*(3), 215–239. https://doi.org/10.1029/gb003i003p00215

Brovkin, V., Ganopolski, A., Archer, D., & Munhoven, G. (2012). Glacial CO_2 cycle as a succession of key physical and biogeochemical processes. *Climate of the Past*, *8*(1), 251–264. https://doi.org/10.5194/cp-8-251-2012

Cartapanis, O., Bianchi, D., Jaccard, S., & Galbraith, E. D. (2016). Global pulses of organic carbon burial in deep-sea sediments during glacial maxima. *Nature Communications*, *7*(1), 10796. https://doi.org/10.1038/ncomms10796

Cartapanis, O., Galbraith, E. D., Bianchi, D., & Jaccard, S. L. (2018). Carbon burial in deep-sea sediment and implications for oceanic inventories of carbon and alkalinity over the last glacial cycle. *Climate of the Past*, *14*(11), 1819–1850. https://doi.org/10.5194/cp-14-1819-2018

Caves, J. K., Jost, A. B., Lau, K. V., & Maher, K. (2016). Cenozoic carbon cycle imbalances and a variable weathering feedback. *Earth and Planetary Science Letters*, *450*, 152–163. https://doi.org/10.1016/j.epsl.2016.06.035

Ciais, P., Sabine, C., Bala, G., Bopp, L., Brovkin, V., Canadell, J., et al. (2013). Carbon and other biogeochemical cycles (Eds.). In *Climate change 2013: The physical science basis. Contribution of working group I to the fifth assessment report of the intergovernmental panel on climate change*. Cambridge University Press.

Clark, P. U., Archer, D., Pollard, D., Blum, J. D., Rial, J. A., Brovkin, V., et al. (2006). The middle Pleistocene transition: Characteristics, mechanisms, and implications for long-term changes in atmospheric pCO_2. *Quaternary Science Reviews*, *25*(23–24), 3150–3184. https://doi.org/10.1016/j.quascirev.2006.07.008

Colbourn, G., Ridgwell, A., & Lenton, T. M. (2013). The rock geochemical model (RokGeM) v0.9. *Geoscientific Model Development*, *6*(5), 1543–1573. https://doi.org/10.5194/gmd-6-1543-2013

Colbourn, G., Ridgwell, A., & Lenton, T. M. (2015). The time scale of the silicate weathering negative feedback on atmospheric CO_2. *Global Biogeochemical Cycles*, *29*(5), 583–596. https://doi.org/10.1002/2014GB005054

Compton, J., Mallinson, D., Glenn, C., Filippelli, G., Föllmi, K., Shields, G., & Zanin, Y. (2000). Variations in the global phosphorus cycle. In *Marine authigenesis: From global to microbial* (pp. 21–33). Wiley-Blackwell.

Deines, P. (2002). The carbon isotope geochemistry of mantle xenoliths. *Earth-Science Reviews*, *58*(3), 247–278. https://doi.org/10.1016/S0012-8252(02)00064-8

Delaney, M. L. (1998). Phosphorus accumulation in marine sediments and the oceanic phosphorus cycle. *Global Biogeochemical Cycles*, *12*(4), 563–572. https://doi.org/10.1029/98GB02263

Edwards, N. R., Willmott, A. J., & Killworth, P. D. (1998). On the role of topography and wind stress on the stability of the thermohaline circulation. *Journal of Physical Oceanography*, *28*(5), 756–778. https://doi.org/10.1175/1520-0485(1998)028⟨0756:OTROTA⟩2.0.CO;2

Eggleston, S., Schmitt, J., Bereiter, B., Schneider, R., & Fischer, H. (2016). Evolution of the stable carbon isotope composition of atmospheric CO_2 over the last glacial cycle. *Paleoceanography*, *31*(3), 434–452. https://doi.org/10.1002/2015PA002874

Emerson, S., & Archer, D. (1992). Glacial carbonate dissolution cycles and atmospheric pCO_2: A view from the ocean bottom. *Paleoceanography*, *7*(3), 319–331. https://doi.org/10.1029/92PA00773

Emerson, S., & Bender, M. (1981). Carbonate fluxes at the sediment-water interface of the deep-sea—Calcium-carbonate preservation. *Journal of Marine Research*, *39*(1), 139–162.

Feely, R. A., Sabine, C. L., Lee, K., Berelson, W., Kleypas, J., Fabry, V. J., & Millero, F. J. (2004). Impact of anthropogenic CO_2 on the $CaCO_3$ system in the oceans. *Science*, *305*(5682), 362–366. https://doi.org/10.1126/science.1097329

Fischer, H., Schmitt, J., Lüthi, D., Stocker, T. F., Tschumi, T., Parekh, P., et al. (2010). The role of Southern Ocean processes in orbital and millennial CO_2 variations—A synthesis. *Quaternary Science Reviews*, *29*(1–2), 193–205. https://doi.org/10.1016/j.quascirev.2009.06.007

Freeman, K. H., & Hayes, J. M. (1992). Fractionation of carbon isotopes by phytoplankton and estimates of ancient CO_2 levels. *Global Biogeochemical Cycles*, *6*(2), 185–198. https://doi.org/10.1029/92GB00190

Ganopolski, A., & Brovkin, V. (2017). Simulation of climate, ice sheets and CO_2 evolution during the last four glacial cycles with an Earth system model of intermediate complexity. *Climate of the Past*, *13*(12), 1695–1716. https://doi.org/10.5194/cp-13-1695-2017

Goericke, R., & Fry, B. (1994). Variations of marine plankton $\delta^{13}C$ with latitude, temperature, and dissolved CO_2 in the world ocean. *Global Biogeochemical Cycles*, *8*(1), 85–90. https://doi.org/10.1029/93GB03272

Goodwin, P., & Ridgwell, A. (2010). Ocean-atmosphere partitioning of anthropogenic carbon dioxide on multimillennial timescales. *Global Biogeochemical Cycles*, *24*(2), GB2014. https://doi.org/10.1029/2008GB003449

Griffies, S. M. (1998). The gent–McWilliams skew flux. *Journal of Physical Oceanography*, *28*(5), 831–841. https://doi.org/10.1175/1520-0485(1998)028⟨0831:TGMSF⟩2.0.CO;2

Hartmann, J., Moosdorf, N., Lauerwald, R., Hinderer, M., & West, A. J. (2014). Global chemical weathering and associated P-release—The role of lithology, temperature and soil properties. *Chemical Geology*, *363*, 145–163. https://doi.org/10.1016/j.chemgeo.2013.10.025

Hasselmann, K., Sausen, R., Maier-Reimer, E., & Voss, R. (1993). On the cold start problem in transient simulations with coupled atmosphere-ocean models. *Climate Dynamics*, *9*(2), 53–61. https://doi.org/10.1007/BF00210008

Hayes, J. M., & Waldbauer, J. R. (2006). The carbon cycle and associated redox processes through time. In *Philosophical transactions of the royal society B—biological sciences*. In *Conference on major steps in cell evolution—Palaeontological, molecular and cellular evidence of their timing and global effects, royal society* (Vol. 361, pp. 931–950). https://doi.org/10.1098/rstb.2006.1840

Heinze, C., Maier-Reimer, E., Winguth, A. M. E., & Archer, D. (1999). A global oceanic sediment model for long-term climate studies. *Global Biogeochemical Cycles*, *13*(1), 221–250. https://doi.org/10.1029/98GB02812

Hoogakker, B. A., Rohling, E. J., Palmer, M. R., Tyrrell, T., & Rothwell, R. G. (2006). Underlying causes for long-term global ocean $\delta^{13}C$ fluctuations over the last 1.20 Myr. *Earth and Planetary Science Letters*, *248*(1–2), 15–29. https://doi.org/10.1016/j.epsl.2006.05.007

Hooss, G., Voss, R., Hasselmann, K., Maier-Reimer, E., & Joos, F. (2001). A nonlinear impulse response model of the coupled carbon cycle-climate system (NICCS). *Climate Dynamics*, *18*(3–4), 189–202. https://doi.org/10.1007/s003820100170

Huybers, P., & Langmuir, C. (2009). Feedback between deglaciation, volcanism, and atmospheric CO_2. *Earth and Planetary Science Letters*, *286*(3–4), 479–491. https://doi.org/10.1016/j.epsl.2009.07.014

Ingall, E., & Jahnke, R. (1994). Evidence for enhanced phosphorus regeneration from marine sediments overlain by oxygen depleted waters. *Geochimica et Cosmochimica Acta*, *58*(11), 2571–2575. https://doi.org/10.1016/0016-7037(94)90033-7

Isson, T. T., Planavsky, N. J., Coogan, L. A., Stewart, E. M., Ague, J. J., Bolton, E. W., et al. (2020). Evolution of the global carbon cycle and climate regulation on Earth. *Global Biogeochemical Cycles*, *34*(2). https://doi.org/10.1029/2018GB006061

Jaccard, S. L., Hayes, C. T., Martinez-Garcia, A., Hodell, D. A., Anderson, R. F., Sigman, D. M., & Haug, G. H. (2013). Two modes of change in southern ocean productivity over the past million years. *Science*, *339*(6126), 1419–1423. https://doi.org/10.1126/science.1227545

Jahn, A., Lindsay, K., Giraud, X., Gruber, N., Otto-Bliesner, B. L., Liu, Z., & Brady, E. C. (2015). Carbon isotopes in the ocean model of the community Earth system model (CESM1). *Geoscientific Model Development*, *8*(8), 2419–2434. https://doi.org/10.5194/gmd-8-2419-2015

Jeltsch-Thömmes, A., Battaglia, G., Cartapanis, O., Jaccard, S. L., & Joos, F. (2019). Low terrestrial carbon storage at the last glacial maximum: Constraints from multi-proxy data. *Climate of the Past*, *15*(2), 849–879. https://doi.org/10.5194/cp-15-849-2019

Jeltsch-Thömmes, A., & Joos, F. (2020). Modeling the evolution of pulse-like perturbations in atmospheric carbon and carbon isotopes: The role of weathering-sedimentation imbalances. *Climate of the Past*, *16*(2), 423–451. https://doi.org/10.5194/cp-16-423-2020

Jeltsch-Thömmes, A., & Joos, F. (2023). Model output from the Bern3D model of 600 kyr weathering step-change experiments [Dataset]. Zenodo. https://doi.org/10.5281/zenodo.7573365

Joos, F., & Bruno, M. (1996). Pulse response functions are cost-efficient tools to model the link between carbon emissions, atmospheric CO_2 and global warming. *Physics and Chemistry of the Earth*, *21*(5–6), 471–476. https://doi.org/10.1016/S0079-1946(97)81144-5

Joos, F., Prentice, I. C., Sitch, S., Meyer, R., Hooss, G., Plattner, G.-K., et al. (2001). Global warming feedbacks on terrestrial carbon uptake under the Intergovernmental Panel on Climate Change (IPCC) emission scenarios. *Global Biogeochemical Cycles*, *15*(4), 891–907. https://doi.org/10.1029/2000GB001375

Joos, F., Roth, R., Fuglestvedt, J. S., Peters, G. P., Enting, I. G., Von Bloh, W., et al. (2013). Carbon dioxide and climate impulse response functions for the computation of greenhouse gas metrics: A multi-model analysis. *Atmospheric Chemistry and Physics*, *13*(5), 2793–2825. https://doi.org/10.5194/acp-13-2793-2013

Jouzel, J., Masson-Delmotte, V., Cattani, O., Dreyfus, G., Falourd, S., Hoffmann, G., et al. (2007). Orbital and millennial Antarctic climate variability over the past 800,000 years. *Science*, *317*(5839), 793–796. https://doi.org/10.1126/science.1141038

Kalnay, E., Kanamitsu, M., Kistler, R., Collins, W., Deaven, D., Gandin, L., et al. (1996). The NCEP/NCAR 40-year reanalysis project. *Bulletin of the American Meteorological Society*, *77*(3), 437–472. https://doi.org/10.1175/1520-0477(1996)077⟨0437:TNYRP⟩2.0.CO;2

Kasting, J. F. (2019). The goldilocks planet? How silicate weathering maintains Earth "Just right". *Elements*, *15*(4), 235–240. https://doi.org/10.2138/gselements.15.4.235

Kemena, T. P., Landolfi, A., Oschlies, A., Wallmann, K., & Dale, A. W. (2019). Ocean phosphorus inventory: Large uncertainties in future projections on millennial timescales and their consequences for ocean deoxygenation. *Earth System Dynamics*, *10*(3), 539–553. https://doi.org/10.5194/esd-10-539-2019

Key, R. M., Kozyr, A., Sabine, C. L., Lee, K., Wanninkhof, R., Bullister, J. L., et al. (2004). A global ocean carbon climatology: Results from Global Data Analysis Project (GLODAP). *Global Biogeochemical Cycles*, *18*(4), 1–23. https://doi.org/10.1029/2004GB002247

Köhler, P., & Munhoven, G. (2020). Late Pleistocene carbon cycle revisited by considering solid Earth processes. *Paleoceanography and Paleoclimatology*, *35*(12), e2020PA004020. https://doi.org/10.1029/2020PA004020

Komar, N., & Zeebe, R. E. (2021). Reconciling atmospheric CO_2, weathering, and calcite compensation depth across the Cenozoic. *Science Advances*, *7*(4), eabd4876. https://doi.org/10.1126/sciadv.abd4876

Kump, L. R., & Alley, R. B. (1994). Global chemical weathering on glacial time scales. *Material Fluxes on the Surface of the Earth*, 46–60.

Lacroix, F., Ilyina, T., & Hartmann, J. (2020). Oceanic CO_2 outgassing and biological production hotspots induced by pre-industrial river loads of nutrients and carbon in a global modeling approach. *Biogeosciences*, *17*(1), 55–88. https://doi.org/10.5194/bg-17-55-2020

Lacroix, F., Ilyina, T., Laruelle, G. G., & Regnier, P. (2021). Reconstructing the preindustrial coastal carbon cycle through a global ocean circulation model: Was the global continental shelf already both autotrophic and a CO_2 sink? *Global Biogeochemical Cycles*, *35*(2), e2020GB006603. https://doi.org/10.1029/2020GB006603

Laws, E. A., Popp, B. N., Bidigare, R. R., Kennicutt, M. C., & Macko, S. A. (1995). Dependence of phytoplankton carbon isotopic composition on growth rate and $[CO_{2,aq}]$: Theoretical considerations and experimental results. *Geochimica et Cosmochimica Acta*, *59*(6), 1131–1138. https://doi.org/10.1016/0016-7037(95)00030-4

Lisiecki, L. E. (2014). Atlantic overturning responses to obliquity and precession over the last 3 Myr. *Paleoceanography*, *29*(2), 71–86. https://doi.org/10.1002/2013PA002505

Lisiecki, L. E., & Raymo, M. E. (2005). A Pliocene-Pleistocene stack of 57 globally distributed benthic $\delta^{18}O$ records. *Paleoceanography*, *20*(1), 1–17. https://doi.org/10.1029/2004PA001071

Liu, B., Six, K. D., & Ilyina, T. (2021). Incorporating the stable carbon isotope ^{13}C in the ocean biogeochemical component of the Max Planck Institute Earth System Model. *Biogeosciences*, *18*(14), 4389–4429. https://doi.org/10.5194/bg-18-4389-2021

Lourantou, A., Chappellaz, J., Barnola, J. M., Masson-Delmotte, V., & Raynaud, D. (2010). Changes in atmospheric CO_2 and its carbon isotopic ratio during the penultimate deglaciation. *Quaternary Science Reviews*, *29*(17–18), 1983–1992. https://doi.org/10.1016/j.quascirev.2010.05.002

Lüthi, D., Le Floch, M., Bereiter, B., Blunier, T., Barnola, J. M., Siegenthaler, U., et al. (2008). High-resolution carbon dioxide concentration record 650,000-800,000 years before present. *Nature*, *453*(7193), 379–382. https://doi.org/10.1038/nature06949

Maier-Reimer, E., & Hasselmann, K. (1987). Transport and storage of CO_2 in the ocean—An inorganic ocean-circulation carbon cycle model. *Climate Dynamics*, *2*(2), 63–90. https://doi.org/10.1007/BF01054491

Marcott, S. A., Bauska, T. K., Buizert, C., Steig, E. J., Rosen, J. L., Cuffey, K. M., et al. (2014). Centennial-scale changes in the global carbon cycle during the last deglaciation. *Nature*, *514*(7524), 616–619. https://doi.org/10.1038/nature13799

Matsumoto, K., Rickaby, R., & Tanioka, T. (2020). Carbon export buffering and CO_2 drawdown by flexible phytoplankton C:N:P under glacial conditions. *Paleoceanography and Paleoclimatology*, *35*(7), e2019PA003823. https://doi.org/10.1029/2019PA003823

Menviel, L., Joos, F., & Ritz, S. P. (2012). Simulating atmospheric CO_2, ^{13}C and the marine carbon cycle during the Last Glacial-Interglacial cycle: Possible role for a deepening of the mean remineralization depth and an increase in the oceanic nutrient inventory. *Quaternary Science Reviews*, *56*, 46–68. https://doi.org/10.1016/j.quascirev.2012.09.012

Metzler, H., Müller, M., & Sierra, C. A. (2018). Transit-time and age distributions for nonlinear time-dependent compartmental systems. *Proceedings of the National Academy of Sciences of the United States of America*, *115*(6), 1150–1155. https://doi.org/10.1073/pnas.1705296115

Meybeck, M. (1982). Carbon, nitrogen, and phosphorous transport by world rivers. *American Journal of Science*, *282*(4), 401–450. https://doi.org/10.2475/ajs.282.4.401

Milliman, J. D., & Droxler, A. W. (1996). Neritic and pelagic carbonate sedimentation in the marine environment: Ignorance is not bliss. *Geologische Rundschau*, *85*(3), 496–504. https://doi.org/10.1007/BF02369004

Mills, B. J. W., Scotese, C. R., Walding, N. G., Shields, G. A., & Lenton, T. M. (2017). Elevated CO_2 degassing rates prevented the return of Snowball Earth during the Phanerozoic. *Nature Communications*, *8*(1), 1110. https://doi.org/10.1038/s41467-017-01456-w

Mook, W. G. (1986). $^{1}3C$ in atmospheric C_O2. *Netherlands Journal of Sea Researc*h, 20(2–3), 211–223. https://doi.org/10.1016/0077-7579(86)90043-8

Müller, S. A., Joos, F., Edwards, N. R., & Stocker, T. F. (2006). Water mass distribution and ventilation time scales in a cost-efficient, three-dimensional ocean model. *Journal of Climate*, *19*(21), 5479–5499. https://doi.org/10.1175/JCLI3911.1

Müller, S. A., Joos, F., Plattner, G. K., Edwards, N. R., & Stocker, T. F. (2008). Modeled natural and excess radiocarbon: Sensitivities to the gas exchange formulation and ocean transport strength. *Global Biogeochemical Cycles*, *22*(3), 1–14. https://doi.org/10.1029/2007GB003065

Munhoven, G. (2002). Glacial—Interglacial changes of continental weathering: Estimates of the related CO_2 and HCO_3—Flux variations and their uncertainties. *Global and Planetary Change*, *33*(1–2), 155–176. https://doi.org/10.1016/S0921-8181(02)00068-1

Munhoven, G., & François, L. M. (1996). Glacial-interglacial variability of atmospheric CO_2 due to changing continental silicate rock weathering: A model study. *Journal of Geophysical Research*, *101*(D16), 21423–21437. https://doi.org/10.1029/96JD01842

Najjar, R. G., & Orr, J. C. (1999). *Biotic-HOWTO. Internal OCMIP (Technical Report). Saclay, Gif-sur-Yvett*e. LSCE/CEA.

Neftel, A., Oeschger, H., Schwander, J., Stauffer, B., & Zumbrunn, R. (1982). Ice core sample measurements give atmospheric CO_2 content during the past 40,000 yr. *Nature*, *295*(5846), 220–223. https://doi.org/10.1038/295220a0

Niemeyer, D., Kemena, T. P., Meissner, K. J., & Oschlies, A. (2016). A model study of warming-induced phosphorus-oxygen feedbacks in open-ocean oxygen minimum zones on millennial timescales. *Earth System Dynamics Discussions*, 1–18. https://doi.org/10.5194/esd-2016-50

Oliver, K. I. C., Hoogakker, B. A. A., Crowhurst, S., Henderson, G. M., Rickaby, R. E. M., Edwards, N. R., & Elderfield, H. (2010). A synthesis of marine sediment core $d^{13}C$ data over the last 150 000 years. *Climate of the Past*, *6*(5), 645–673. https://doi.org/10.5194/cp-6-645-2010

Orr, J. C., & Epitalon, J. M. (2015). Improved routines to model the ocean carbonate system: Mocsy 2.0. *Geoscientific Model Development*, *8*(3), 485–499. https://doi.org/10.5194/gmd-8-485-2015

Palastanga, V., Slomp, C. P., & Heinze, C. (2011). Long-term controls on ocean phosphorus and oxygen in a global biogeochemical model. *Global Biogeochemical Cycles*, *25*(3), 1–19. https://doi.org/10.1029/2010GB003827

Parekh, P., Joos, F., & Müller, S. A. (2008). A modeling assessment of the interplay between aeolian iron fluxes and iron-binding ligands in controlling carbon dioxide fluctuations during Antarctic warm events. *Paleoceanography*, *23*(4), PA4202. https://doi.org/10.1029/2007PA001531

Paulmier, A., Kriest, I., & Oschlies, A. (2009). Stoichiometries of remineralisation and denitrification in global biogeochemical ocean models. *Biogeosciences*, *6*(5), 923–935. https://doi.org/10.5194/bg-6-923-2009

Peterson, C. D., & Lisiecki, L. E. (2018). Deglacial carbon cycle changes observed in a compilation of 127 benthic $d^{13}C$ time series (20-6 ka). *Climate of the Past*, *14*(8), 1229–1252. https://doi.org/10.5194/cp-14-1229-2018

Peterson, C. D., Lisiecki, L. E., & Stern, J. V. (2014). Deglacial whole-ocean $d^{13}C$ change estimated from 480 benthic foraminiferal records. *Paleoceanography*, *29*(6), 549–563. https://doi.org/10.1002/2013PA002552

Peterson, L. C., & Prell, W. L. (1985). Carbonate preservation and rates of climatic change: An 800 kyr record from the Indian Ocean. In *The carbon cycle and atmospheric CO_2: Natural variations archean to present* (pp. 251–269). American Geophysical Union (AGU). https://doi.org/10.1029/GM032p0251

Popp, B. N., Takigiku, R., Hayes, J. M., Louda, J. W., & Baker, E. W. (1989). The post-Paleozoic chronology and mechanism of 13 C depletion in primary marine organic matter. *American Journal of Science*, *289*(4), 436–454. https://doi.org/10.2475/ajs.289.4.436

Ramirez, A. J., & Rose, A. W. (1992). Analytical geochemistry of organic phosphorus and its correlation with organic carbon in marine and fluvial sediments and soils. *American Journal of Science*, *292*(6), 421–454. https://doi.org/10.2475/ajs.292.6.421

Raymo, M. E., Oppo, D. W., & Curry, W. (1997). The mid-pleistocene climate transition: A deep sea carbon isotopic perspective. *Paleoceanography*, *12*(4), 546–559. https://doi.org/10.1029/97PA01019

Regnier, P., Friedlingstein, P., Ciais, P., Mackenzie, F. T., Gruber, N., Janssens, I. A., et al. (2013). Anthropogenic perturbation of the carbon fluxes from land to ocean. *Nature Geoscience*, *6*(8), 597–607. https://doi.org/10.1038/NGEO1830

Ridgwell, A., & Zeebe, R. (2005). The role of the global carbonate cycle in the regulation and evolution of the Earth system. *Earth and Planetary Science Letters*, *234*(3–4), 299–315. https://doi.org/10.1016/j.epsl.2005.03.006

Ritz, S., Stocker, T. F., & Joos, F. (2011). A coupled dynamical ocean-energy balance atmosphere model for paleoclimate studies. *Journal of Climate*, *24*(2), 349–375. https://doi.org/10.1175/2010JCLI3351.1

Roth, R., & Joos, F. (2012). Model limits on the role of volcanic carbon emissions in regulating glacial-interglacial CO_2variations. *Earth and Planetary Science Letters*, *329–330*, 141–149. https://doi.org/10.1016/j.epsl.2012.02.019

Roth, R., Ritz, S. P., & Joos, F. (2014). Burial-nutrient feedbacks amplify the sensitivity of atmospheric carbon dioxide to changes in organic matter remineralisation. *Earth System Dynamics*, *5*(2), 321–343. https://doi.org/10.5194/esd-5-321-2014

Rugenstein, J. K. C., Ibarra, D. E., & von Blanckenburg, F. (2019). Neogene cooling driven by land surface reactivity rather than increased weathering fluxes. *Nature*, *571*(7763), 99+–102. https://doi.org/10.1038/s41586-019-1332-y

Sarmiento, J. L., & Gruber, N. (2006). *Ocean biogeochemical dynamics*. Princeton University Press.

Sarmiento, J. L., Orr, J. C., & Siegenthaler, U. (1992). A perturbation simulation of CO_2 uptake in an ocean general circulation model. *Journal of Geophysical Research*, *97*(C3), 3621–3645. https://doi.org/10.1029/91JC02849

Schmitt, J., Schneider, R., Elsig, J., Leuenberger, D., Lourantou, a., Chappellaz, J., et al. (2012). Carbon isotope constraints on the deglacial CO_2 rise from ice cores. *Science*, *336*(6082), 711–714. https://doi.org/10.1126/science.1217161

Schmittner, A., Gruber, N., Mix, A. C., Key, R. M., Tagliabue, A., & Westberry, T. (2013). Biology and air–sea gas exchange controls on the distribution of carbon isotope ratios ($d^{13}C$) in the ocean. *Biogeosciences*, *10*(9), 5793–5816. https://doi.org/10.5194/bg-10-5793-2013

Schneider, R., Schmitt, J., Köhler, P., Joos, F., & Fischer, H. (2013). A reconstruction of atmospheric carbon dioxide and its stable carbon isotopic composition from the penultimate glacial maximum to the last glacial inception. *Climate of the Past*, *9*(6), 2507–2523. https://doi.org/10.5194/cp-9-2507-2013

Schrag, D. P., Higgins, J. A., Macdonald, F. A., & Johnston, D. T. (2013). Authigenic carbonate and the history of the global carbon cycle. *Science*, *339*(6119), 540–543. https://doi.org/10.1126/science.1229578

Siegenthaler, U., & Muennich, K. O. (1981). Carbon-13/carbon-12 fractionation during carbon dioxide transfer from air to sea. In B. Bolin (Ed.), *Scope 16: Carbon cycle modelling* (pp. 249–257). Wiley.

Siegenthaler, U., & Oeschger, H. (1987). Biospheric CO_2 emissions during the past 200 years reconstructed by deconvolution of ice core data. *Tellus B: Chemical and Physical Meteorology*, *39*(1–2), 140–154. https://doi.org/10.3402/tellusb.v39i1-2.15331

Siegenthaler, U., Stocker, T. F., Monnin, E., Lüthi, D., Schwander, J., Stauffer, B., et al. (2005). Stable carbon cycle-climate relationship during the late pleistocene. *Science*, *310*(5752), 1313–1317. https://doi.org/10.1126/science.1120130

Sigman, D. M., & Boyle, E. A. (2000). Glacial/interglacial variations in atmospheric carbon dioxide. *Nature*, *407*(6806), 859–869. https://doi.org/10.1038/35038000

Sigman, D. M., Hain, M. P., & Haug, G. H. (2010). The polar ocean and glacial cycles in atmospheric CO_2 concentration. *Nature*, *466*(7302), 47–55. https://doi.org/10.1038/nature09149

Sigman, D. M., McCorkle, D. C., & Martin, W. R. (1998). The calcite lysocline as a constraint on glacial/interglacial low-latitude production changes. *Global Biogeochemical Cycles*, *12*(3), 409–427. https://doi.org/10.1029/98GB01184

Stolper, D. A., Bender, M. L., Dreyfus, G. B., Yan, Y., & Higgins, J. A. (2016). A Pleistocene ice core record of atmospheric O_2 concentrations. *Science*, *353*(6306), 1427–1430. https://doi.org/10.1126/science.aaf5445

Strassmann, K. M., & Joos, F. (2018). The Bern simple climate model (BernSCM) v1.0: An extensible and fully documented open-source re-implementation of the Bern reduced-form model for global carbon cycle-climate simulations. *Geoscientific Model Development*, *11*(5), 1887–1908. https://doi.org/10.5194/gmd-11-1887-2018

Suchet, P., & Probst, J. (1995). A global-model for present day atmospheric soil CO_2 consumption by chemical erosion of continental rocks (GEM-CO2). In *Tellus series B—Chemical and physical meteorology* (Vol. 47, pp. 273–280). *4th Atmospheric CO(2) International Conference*. https://doi.org/10.1034/j.1600-0889.47.issue1.23.x

Thompson, M., & Randerson, J. (1999). Impulse response functions of terrestrial carbon cycle models: Method and application. *Global Change Biology*, *5*(4), 371–394. https://doi.org/10.1046/j.1365-2486.1999.00235.x

Tierney, J. E., Zhu, J., King, J., Malevich, S. B., Hakim, G. J., & Poulsen, C. J. (2020). Glacial cooling and climate sensitivity revisited. *Nature*, *584*(7822), 569–573. https://doi.org/10.1038/s41586-020-2617-x

Tréguer, P. J., Sutton, J. N., Brzezinski, M., Charette, M. A., Devries, T., Dutkiewicz, S., et al. (2021). Reviews and syntheses: The biogeochemical cycle of silicon in the modern ocean. *Biogeosciences*, *18*(4), 1269–1289. https://doi.org/10.5194/bg-18-1269-2021

Tschumi, T., Joos, F., Gehlen, M., & Heinze, C. (2011). Deep ocean ventilation, carbon isotopes, marine sedimentation and the deglacial CO_2 rise. *Climate of the Past*, *7*(3), 771–800. https://doi.org/10.5194/cp-7-771-2011

Van Cappellen, P., & Ingall, E. D. (1994). Benthic phosphorus regeneration, net primary production, and ocean anoxia: A model of the coupled marine biogeochemical cycles of carbon and phosphorus. *Paleoceanography*, *9*(5), 677–692. https://doi.org/10.1029/94PA01455

Walker, J. C. G., Hays, P. B., & Kasting, J. F. (1981). A negative feedback mechanism for the long-term stabilization of Earth's surface temperature. *Journal of Geophysical Research*, *86*(C10), 9776–9782. https://doi.org/10.1029/JC086iC10p09776

Wallmann, K. (2010). Phosphorus imbalance in the global ocean? *Global Biogeochemical Cycles*, *24*(4), GB4030. https://doi.org/10.1029/2009GB003643

Wallmann, K. (2014). Is late Quaternary climate change governed by self-sustained oscillations in atmospheric CO_2? *Geochimica et Cosmochimica Acta*, *132*, 413–439. https://doi.org/10.1016/j.gca.2013.10.046

Wallmann, K., Schneider, B., & Sarnthein, M. (2016). Effects of eustatic sea-level change, ocean dynamics, and nutrient utilization on atmospheric pCO_2 and seawater composition over the last 130 000 years: A model study. *Climate of the Past*, *12*(2), 339–375. https://doi.org/10.5194/cp-12-339-2016

Wanninkhof, R. (2014). Relationship between wind speed and gas exchange over the ocean revisited. *Limnology and Oceanography: Methods*, *12*(6), 351–362. https://doi.org/10.4319/lom.2014.12.351

Watson, B. A. J. (2016). Oceans on the edge of anoxia. *Science*, *354*(6319), 1529–1530. https://doi.org/10.1126/science.aaj2321

Willeit, M., Ganopolski, A., Calov, R., & Brovkin, V. (2019). Mid-Pleistocene transition in glacial cycles explained by declining CO_2 and regolith removal. *Science Advances*, *5*(4). https://doi.org/10.1126/sciadv.aav7337

Willeit, M., Ganopolski, A., Robinson, A., & Edwards, N. R. (2022). The Earth system model CLIMBER-X v1.0 – Part 1: Climate model description and validation. *Geoscientific Model Development*, *15*(14), 5905–5948. https://doi.org/10.5194/gmd-15-5905-2022

Yu, J., Anderson, F., & Rohling, E. J. (2014). Deep Ocean carbonate chemistry and glacial-interglacial atmospheric CO_2 changes. *Oceanography*, *27*(1), 16–25. https://doi.org/10.5670/oceanog.2011.65